



This discussion paper is/has been under review for the journal Geoscientific Model Development (GMD). Please refer to the corresponding final paper in GMD if available.

ASAM v2.7: a compressible atmospheric model with a Cartesian cut cell approach

M. Jähn, O. Knoth, M. König, and U. Vogelsberg

Leibniz Institute for Tropospheric Research, Permoserstrasse 15, 04318 Leipzig, Germany

Received: 16 June 2014 – Accepted: 27 June 2014 – Published: 18 July 2014

Correspondence to: M. Jähn (jaehn@tropos.de)

Published by Copernicus Publications on behalf of the European Geosciences Union.

Title Page

Abstract

Introduction

Conclusions

References

Tables

Figures



Back

Close

Full Screen / Esc

Printer-friendly Version

Interactive Discussion



Abstract

In this work, the fully compressible, nonhydrostatic atmospheric model ASAM is presented. A cut cell approach is used to include obstacles and orography into the Cartesian grid. Discretization is realized by a mixture of finite differences and finite volumes and a state limiting is applied. An implicit time integration scheme ensures numerical stability around small cells. To make the model applicable for atmospheric problems, physical parameterizations like a Smagorinsky subgrid scale model, a two-moment bulk microphysics scheme, precipitation and vertical surface fluxes by a constant flux layer or a more complex soil model are implemented. Results for three benchmark test cases from the literature are shown. A sensitivity study regarding the development of a convective boundary layer together with island effects at Barbados is carried out to show the capability to perform real case simulations with ASAM.

1 Introduction

In this paper we present the numerical solver ASAM (All Scale Atmospheric Model) that has been developed at the Leibniz Institute for Tropospheric Research (TROPOS), Leipzig. ASAM was initially designed for CFD (Computational Fluid Dynamics) simulations around buildings where obstacles are included within a Cartesian grid by a cut cell method. This approach is also used to include real orographic data in the model domain. With this attempt one remains within the Cartesian grid and no artificial forces in the vicinity of an obstacle or topographic structure occur in comparison to other coordinate systems like terrain-following coordinates (Lock et al., 2012). Several techniques have been developed to overcome these non-physical errors, especially when spatial scales of three-dimensional models become finer. Tripoli and Smith (2014a) introduced a Variable-Step Topography (VST) surface coordinate system within a nonhydrostatic host model. Unlike the traditional discrete-step approach, the depth of a grid box intersecting with a topographical structure is adjusted to its height, which leads to straight

GMDD

7, 4463–4525, 2014

ASAM v2.7

M. Jähn et al.

Title Page

Abstract

Introduction

Conclusions

References

Tables

Figures

⏪

⏩

◀

▶

Back

Close

Full Screen / Esc

Printer-friendly Version

Interactive Discussion



[Title Page](#)[Abstract](#)[Introduction](#)[Conclusions](#)[References](#)[Tables](#)[Figures](#)[◀](#)[▶](#)[◀](#)[▶](#)[Back](#)[Close](#)[Full Screen / Esc](#)[Printer-friendly Version](#)[Interactive Discussion](#)

cut cells. Numerical tests show that this technique produce better results than the conventional approaches for different topography (severe and smooth) types (Tripoli and Smith, 2014b). In their cases, also the computational costs with the VST approach are reduced because there is no need of extra functional transform calculations due to metric terms. Steppeler et al. (2002) derived approximations for z coordinate nonhydrostatic atmospheric models by using the shaved-element finite-volume method. There, the dynamics are computed in the cut cell system, whereas the physics computation remains in the terrain-following system. The cut cell method is also used in the Ocean–Land–Atmosphere Model (OLAM) (Walko and Avissar, 2008a), which extends the Regional Atmospheric Modeling System (RAMS) to a global model domain. In OLAM, the shaved-cell method is applied to an icosahedral mesh (Walko and Avissar, 2008b). When using cut cells, no matter what particular scheme, low-volume cells will always be generated. To avoid instability problems around these small cells, the time integration scheme has to be adapted. For this, linear-implicit Rosenbrock time integration schemes are used in ASAM.

The here presented model is a developing research code and has a lot of different options to choose like different numerical methods (e.g. split-explicit Runge–Kutta schemes), number of prognostic variables, physical parameterizations or the change to spherical grid types. ASAM is a fully parallelized software using the Message Passing Interface (MPI) and the domain decomposition method. The code is easily portable between different platforms like Linux, IBM or Mac OS. With these features, large eddy simulations (LES) with spatial resolutions of $\mathcal{O}(100\text{ m})$ can be performed with respect to a sufficiently resolved terrain structure. The model was recently used for a study of dynamic flow structures in a turbulent urban environment of a building-resolving resolution (König, 2013).

A separately developed LES model at TROPOS is called ASAMgpu (Horn, 2012). It includes some basic features of the ASAM code and runs on graphics processing units (GPUs), which enables very time-efficient computations and post-processing. However,

this model is not as adjustable as the original ASAM code and the inclusion of three-dimensional orographical structures is not implemented so far.

This paper is structured as follows. The next section deals with a general description of the model. It includes the basic equations that are solved numerically and the used energy variable. Also, the cut cell approach and spatial discretization as well as the used time integration scheme are described. In Sect. 3, mandatory physical parameterizations for LES like subgrid scale model, microphysics etc. are presented. Results of three two-dimensional benchmark test cases are shown in Sect. 4. The first one is a cold bubble that sinks down and creates a density current as described in Straka et al. (1993). A moist rising bubble case in a supersaturated environment by Bryan and Fritsch (2002) has been chosen to show the effects of latent heat release and the condensation process. To demonstrate the capability of the cut cell method, the results of a third case with simulated flow around an idealized row of mountains and a subsequent generation of gravity waves are presented (Schaer et al., 2002). Some more complex simulations are performed in Sect. 5. There, a 3-D LES sensitivity study dealing with island effects at the Caribbean island Barbados (13°06' N, 59°37' W) is done. The island shape and topography are directly included in the grid. An analysis of the terrain effect and changes in wind speed and moisture load is carried out. Section 6 describes how to get access to the model code and which visualization software is used followed by concluding remarks in the final section.

2 Description of the All Scale Atmospheric Model

2.1 Governing equations

The flux-form compressible Euler equations for the atmosphere are

$$\frac{\partial \rho}{\partial t} + \nabla \cdot (\rho \mathbf{v}) = 0 \quad (1)$$



$$\frac{\partial(\rho \mathbf{v})}{\partial t} + \nabla \cdot (\rho \mathbf{v} \mathbf{v}) = -\nabla p - \rho \mathbf{g} - 2\boldsymbol{\Omega} \times (\rho \mathbf{v}) \quad (2)$$

$$\frac{\partial(\rho \phi)}{\partial t} + \nabla \cdot (\rho \mathbf{v} \phi) = S_\phi \quad (3)$$

where ρ is the total air density, $\mathbf{v} = (u, v, w)^T$ the three-dimensional velocity vector, p the air pressure, \mathbf{g} the gravitational acceleration, $\boldsymbol{\Omega}$ the angular velocity vector of the earth, ϕ a scalar quantity and S_ϕ the sum of its corresponding source terms.

The energy equation in the form of Eq. (3) is represented by the (dry) potential temperature θ . In the presence of water vapor and cloud water, this quantity is replaced by the density potential temperature θ_ρ (Emanuel, 1994) as a more generalized form of the virtual potential temperature θ_v :

$$\theta_\rho = \theta \left(1 + q_v \left[\frac{R_v}{R_d} - 1 \right] - q_c \right) \quad (4)$$

where the equation of state can be expressed as follows:

$$\rho = \rho_0 R_d \theta_\rho \left(\frac{\rho}{\rho_0} \right)^{\kappa_m} \quad (5)$$

In the above two equations $\theta = T(\rho_0/\rho)^{\kappa_m}$ is the potential temperature, $q_v = \rho_v/\rho$ is the mass ratio of water vapor in the air (specific humidity), $q_c = \rho_c/\rho$ is the mass ratio of cloud water in the air, ρ_0 a reference pressure and $\kappa_m = (q_d R_d + q_v R_v)/(q_d c_{pd} + q_v c_{pv} + q_c c_{pl})$ the Poisson constant for the air mixture (dry air, water vapor, cloud water) with $q_d = \rho_d/\rho$. R_d and R_v are the gas constants for dry air and water vapor, respectively.

The number of additional equations like Eq. (3) depends on the complexity of the used microphysical scheme. Furthermore, tracer variables can also be included. The values of all relevant physical constants are listed in Table 1.

Title Page

Abstract

Introduction

Conclusions

References

Tables

Figures

◀

▶

◀

▶

Back

Close

Full Screen / Esc

Printer-friendly Version

Interactive Discussion



2.2 Cut cells and spatial discretization

The spatial discretization is done on a Cartesian grid with grid intervals of lengths $\Delta x_i, \Delta y_j, \Delta z_k$ and can easily be extended to any logically orthogonal rectangular grid like spherical or cylindrical coordinates. First, it is described for the Cartesian case.

Generalizations are discussed afterwards. Orography and other obstacles like buildings are presented by cut cells, which are the result of the intersection of the obstacle with the underlying Cartesian grid. In Fig. 1 different possible configurations are shown for the three-dimensional case. For each Cartesian cell, the free face area of the six faces and the free volume area of the cell are stored. This is the part that is outside of the obstacle. These values are denoted for the grid cell i, j, k by $FU_{i-1/2,j,k}, FU_{i+1/2,j,k}, FV_{i,j-1/2,k}, FV_{i,j+1/2,k}, FW_{i,j,k-1/2}, FW_{i,j,k+1/2}, V_{i,j,k}$ respectively. In the following, the relative notations FU_L and FU_R are used, e.g. as shown in Fig. 2.

The spatial discretization is formulated in terms of the grid interval length and the face and volume areas. The variables are arranged on a staggered grid with momentum at the cell faces and all other variables at the cell center. The discretization is a mixture of finite volumes and finite differences. In the finite volume context the main task is the reconstruction of values and gradients at cell faces from cell centered values.

The discretization of the advection operator is performed for a generic cell centered scalar variable ϕ . In the context of a finite volume discretization point values of the scalar value ϕ are needed at the faces of this grid cell. Knowing these face values, the advection operator in U direction is discretized by $(FU_R UF_R \phi_R - FU_L UF_L \phi_L) / V_C$. To approximate these values at the faces, a biased upwind third-order procedure with additional limiting is used (Van Leer, 1994).

Assuming a positive flow in the x direction, the third order approximation at $x_{i+1/2}$ is obtained by quadratic interpolation from the three values as shown in Fig. 3. The interpolation condition is that the three cell-averaged values are fitted:

Title Page

Abstract

Introduction

Conclusions

References

Tables

Figures

⏪

⏩

◀

▶

Back

Close

Full Screen / Esc

Printer-friendly Version

Interactive Discussion



[Title Page](#)
[Abstract](#)
[Introduction](#)
[Conclusions](#)
[References](#)
[Tables](#)
[Figures](#)
[◀](#)
[▶](#)
[◀](#)
[▶](#)
[Back](#)
[Close](#)
[Full Screen / Esc](#)
[Printer-friendly Version](#)
[Interactive Discussion](#)


$$\begin{aligned}\phi_{FR} &= \phi_C + \frac{h_C(h_L + h_C)}{(h_C + h_R)(h_L + h_C + h_R)}(\phi_R - \phi_C) + \frac{h_C h_R}{(h_L + h_C)(h_L + h_C + h_R)}(\phi_C - \phi_L) \\ &= \phi_C + \alpha_1(\phi_R - \phi_C) + \alpha_2(\phi_C - \phi_L).\end{aligned}\quad (6)$$

To achieve positivity in Eq. (6), we apply state limiting. For this task (Eq. 6) is rewritten in slope-ratio formulation

$$\phi_{FR} = \phi_C + K(\phi_C - \phi_L)\quad (7)$$

where

$$K = \alpha_1 \frac{\phi_R - \phi_C}{\phi_C - \phi_L} + \alpha_2.\quad (8)$$

Then K is replaced by the limiter

$$\phi = \max\left(0, \min\left[\frac{\phi_R - \phi_C}{\phi_C - \phi_L}, \min(\delta, K)\right]\right), \quad \delta = 2\quad (9)$$

as proposed by Sweby (1984). This limiter has the property that the unlimited higher order scheme (Eq. 6) is used as much as possible and it is utilized only then when it is needed. In the case of $\phi = 0$, the scheme degenerates to the simple first-order upwind scheme. The coefficients α_1 and α_2 can be computed in advance to minimize the overhead for a non-uniform grid. In the case of a uniform grid the coefficients are constant, i.e. they are equal to $1/3$ and $1/6$. For a detailed discussion of the benefits of this approach and numerical experiments also see Hundsdorfer et al. (1995).

This procedure is applied in all three grid directions, where the virtual grid sizes h are defined by

$$h_L = V_L / F_L\quad (10)$$

$$h_C = 0.5V_C / (F_L + F_R)\quad (11)$$

$$h_R = V_R / F_R \quad (12)$$

To solve the momentum equation, the non-linear advection term is needed on the face. This is achieved by a shifting technique introduced by Hicken et al. (2005) for the incompressible Navier–Stokes-Equation. For each cell two cell-centered values of each of the three components of the cartesian velocity vector are computed and transported with the above advection scheme for a cell-centered scalar value. The obtained tendencies are then interpolated back to the faces. For a normal cell the shifted values are obtained from the six momentum face values, whereas for a cut cell the shift operation takes into account the weights of the faces of the two opposite sides.

$$U_{LC} = \begin{cases} UF_L & \text{if } FU_L \geq FU_R \\ UF_L FU_L + UF_R (FU_R - FU_L) / FU_R & \text{else.} \end{cases} \quad (13)$$

The tendency interpolation from cells (TU_{LC} , TU_{RC}) to a face (TU_F) is obtained by the arithmetic mean of the two tendencies of the two shifted cell components originated from the same face. For a cut face the interpolation takes the form

$$TU_F = \left(\frac{V_R TU_{LC}}{FU_R + FU_C} + \frac{V_L TU_{RC}}{FU_L + FU_C} \right) FU_C. \quad (14)$$

The pressure gradient and the Buoyancy term are computed for all faces with standard difference and interpolation formulas with the grid sizes taken from the underlying Cartesian grid.

2.3 Time integration

After spatial discretization an ordinary differential equation

$$y(t)' = F(y(t)) \quad (15)$$

Title Page

Abstract

Introduction

Conclusions

References

Tables

Figures

◀

▶

◀

▶

Back

Close

Full Screen / Esc

Printer-friendly Version

Interactive Discussion



is obtained that has to be integrated in time (method of lines). To tackle the small time step problem connected with tiny cut cells, linear implicit Rosenbrock-W-methods are used (Jebens et al., 2011).

A Rosenbrock method has the form

$$5 \quad (\mathbf{I} - \tau\gamma\mathbf{J})k_i = \tau F(y_n + \sum_{j=1}^{i-1} \alpha_{ij}u_j) + \sum_{j=1}^{i-1} \beta_{ij}k_j, \quad i = 1, \dots, s \quad (16)$$

$$y_{n+1} = y_n + \sum_{j=1}^s \alpha_{s+1j}k_j,$$

where y_n is a given approximation at $y(t)$ at time t_n and subsequently y_{n+1} at time $t_{n+1} = t_n + \tau$. In addition \mathbf{J} is an approximation to the Jacobian matrix $\partial F/\partial y$. A Rosenbrock method is therefore fully described by the two matrices $\mathbf{A} = (\alpha_{ij})$, $\mathbf{\Gamma} = (\gamma_{ij})$ and the parameter γ .

Among the available methods are a second order two stage method after Lanser et al. (2001).

$$\mathbf{S}k_1 = \tau F(y_n), \quad (17)$$

$$15 \quad \mathbf{S}k_2 = \tau F\left(y_n + \frac{2}{3}k_1\right) - \frac{4}{3}k_1, \quad (18)$$

$$y_{n+1} = y_n + \frac{5}{4}k_1 + \frac{3}{4}k_2, \quad (19)$$

$$\mathbf{S} = \mathbf{I} - \gamma\tau\mathbf{J}, \quad \mathbf{J} \approx F'(y_n). \quad (20)$$

with $\gamma = \frac{1}{2} + \frac{1}{6}\sqrt{3}$ or in matrix form in Table 2.

20 A second method was constructed from a low storage three stage second-order Runge–Kutta method, which is used in split-explicit time integration methods in the Weather Research and Forecasting (WRF) Model (Skamarock et al., 2008) or in the

Title Page

Abstract

Introduction

Conclusions

References

Tables

Figures

◀

▶

◀

▶

Back

Close

Full Screen / Esc

Printer-friendly Version

Interactive Discussion



Consortium for Small-scale Modeling (COSMO) model (Doms et al., 2011). Its coefficients are given in Table 3.

The above described Rosenbrock-W-methods allows a simplified solution of the linear systems without losing the order. When $\mathbf{J} = \mathbf{J}_A + \mathbf{J}_B$ the matrix \mathbf{S} can be replaced by $\mathbf{S} = (\mathbf{I} - \gamma\tau\mathbf{J}_A)(\mathbf{I} - \gamma\tau\mathbf{J}_B)$. Further simplification can be reached by omitting some parts of the Jacobian or by replacing of the derivatives by the same derivatives of a simplified operator $\tilde{F}(w^n)$. For instance higher-order interpolation formula are replaced by the first-order upwind method. The structure of the Jacobian is

$$\mathbf{J} = \begin{pmatrix} \frac{\partial F_\rho}{\partial \rho} & \frac{\partial F_\rho}{\partial V} & 0 \\ \frac{\partial F_V}{\partial \rho} & \frac{\partial F_V}{\partial V} & \frac{\partial F_V}{\partial \Theta} \\ 0 & \frac{\partial F_\Theta}{\partial V} & \frac{\partial F_\Theta}{\partial \Theta} \end{pmatrix}. \quad (21)$$

A zero block 0 indicates that this block is not included in the Jacobian or is absent. The derivative with respect to ρ is only taken for the buoyancy term in the vertical momentum equation. Note that this type of approximation is the standard approach in the derivation of the Boussinesq approximation starting from the compressible Euler equations. The matrix \mathbf{J} can be decomposed as

$$\mathbf{J} = \mathbf{J}_T + \mathbf{J}_P = \begin{pmatrix} \frac{\partial F_\rho}{\partial \rho} & 0 & 0 \\ \frac{\partial F_V}{\partial \rho} & \frac{\partial F_V}{\partial V} & 0 \\ 0 & 0 & \frac{\partial F_\Theta}{\partial \Theta} \end{pmatrix} + \begin{pmatrix} 0 & \frac{\partial F_\rho}{\partial V} & 0 \\ 0 & 0 & \frac{\partial F_V}{\partial \Theta} \\ 0 & \frac{\partial F_\Theta}{\partial V} & 0 \end{pmatrix} \quad (22)$$

or

$$\mathbf{J} = \mathbf{J}_T + \mathbf{J}_P = \begin{pmatrix} \frac{\partial F_\rho}{\partial \rho} & 0 & 0 \\ 0 & \frac{\partial F_V}{\partial V} & 0 \\ 0 & 0 & \frac{\partial F_\Theta}{\partial \Theta} \end{pmatrix} + \begin{pmatrix} 0 & \frac{\partial F_\rho}{\partial V} & 0 \\ \frac{\partial F_V}{\partial \rho} & 0 & \frac{\partial F_V}{\partial \Theta} \\ 0 & \frac{\partial F_\Theta}{\partial V} & 0 \end{pmatrix}. \quad (23)$$

Title Page

Abstract

Introduction

Conclusions

References

Tables

Figures



Back

Close

Full Screen / Esc

Printer-friendly Version

Interactive Discussion



[Title Page](#)[Abstract](#)[Introduction](#)[Conclusions](#)[References](#)[Tables](#)[Figures](#)[◀](#)[▶](#)[◀](#)[▶](#)[Back](#)[Close](#)[Full Screen / Esc](#)[Printer-friendly Version](#)[Interactive Discussion](#)

The first part of the splitting \mathbf{J}_T is called the transport/source part and contains the advection, diffusion and source terms like Coriolis, curvature, Buoyancy, latent heat, and so on. The second matrix is called the pressure part and involves the pressure gradient and the derivative of the divergence with respect to momentum of the density and potential temperature equation. The difference between the two splitting approaches is the insertion of the derivative of the gravity term in the transport or pressure matrix. The first splitting (Eq. 22) damps sound waves and can be reduced to a Poisson-like equation, whereas the second splitting (Eq. 23) damps sound and gravity waves but the dimension of the system is doubled. Both systems are solved by preconditioned conjugate gradient (CG)-like methods. The transport/source system

$$(\mathbf{I} - \gamma\tau\mathbf{J}_{AD} - \gamma\tau\mathbf{J}_S)\Delta W = R \quad (24)$$

is preconditioned from the right with the matrix

$$\mathbf{P}_r = (\mathbf{I} - \gamma\tau\mathbf{J}_{AD})^{-1} \quad (25)$$

and from the left with the matrix

$$\mathbf{P}_l = (\mathbf{I} - \gamma\tau\mathbf{J}_S)^{-1}. \quad (26)$$

where the matrix \mathbf{J}_{AD} is the derivative of the advection and diffusion operator where the unknowns are coupled between grid cells. The matrix \mathbf{J}_S assembles the source terms. Here the coupling is between the unknowns of different components in each grid cell. The matrix

$$\mathbf{P}_l(\mathbf{I} - \gamma\tau\mathbf{J}_{AD} - \gamma\tau\mathbf{J}_S)\mathbf{P}_r \quad (27)$$

can be written in the following form by using the Eisenstat trick:

$$(\mathbf{I} - \gamma\tau\mathbf{P}_l\mathbf{J}_{AD})\mathbf{P}_r = (\mathbf{I} + \mathbf{P}_l((\mathbf{I} - \gamma\tau\mathbf{J}_{AD}) + \mathbf{I}))\mathbf{P}_r. \quad (28)$$

Therefore only the LU-decomposition of the matrix $(\mathbf{I} - \gamma\tau\mathbf{J}_S)$ has to be stored. The matrix $(\mathbf{I} - \gamma\tau\mathbf{J}_{AD})$ is inverted by a fixed number of Gauss–Seidel iterations. In the parallel case we use one cell overlap.

The second matrix of the splitting approach writes in case of the first splitting (Eq. 22) as follows:

$$(\mathbf{I} - \gamma\tau\mathbf{J}_P) = \begin{pmatrix} \mathbf{V}_F & \gamma\tau\text{GRADD}\mathbf{D}_\Theta \\ \gamma\tau\text{DIV}\mathbf{D}_V & \mathbf{V}_C \end{pmatrix}, \quad (29)$$

where \mathbf{V}_F , \mathbf{V}_C , \mathbf{D}_V , and \mathbf{D}_Θ are diagonal matrices. Elimination of the momentum part gives a Helmholtz equation for the increment of the potential temperature. This equation is solved by a CG-method with a multigrid as a preconditioner. For the second splitting (Eq. 23) the resulting matrix is twice in dimension and not symmetric anymore.

Furthermore, different types of split-explicit time integration methods are available, which are especially suitable for simulations without orography methods like large eddy simulations over flat water surfaces (Wensch et al., 2009; Knoth and Wensch, 2014).

3 Physical parameterizations

3.1 Smagorinsky subgrid-scale model

The set of coupled differential equations can be solved for a given flow problem by using mathematical methods. For simulating turbulent flows with large eddy simulation, the Euler equations mentioned above have to be modified. The main purpose for LES is to reduce the computational simulation costs. For that, it is necessary to characterize the unresolved motion. By solving Eqs. (1)–(3) numerically with a grid size, which is above the size of the smallest turbulent scales, the equations have to be filtered. Large eddy simulation employs a spatial filter to separate the large scale motion from the small scales. Large eddies are resolved explicitly by the prognostic Euler equations down to a pre-defined filter-scale Δ , while smaller scales have to be modeled. Due to

Title Page

Abstract

Introduction

Conclusions

References

Tables

Figures



Back

Close

Full Screen / Esc

Printer-friendly Version

Interactive Discussion



the filtering operation, additional terms that cannot be derived trivially occur in the set of Euler equation.

Nevertheless, to solve the filtered set of equations, it is necessary to parameterize the additional subgrid-scale stress terms $\tau_{ij} = \overline{u_i u_j} - \overline{u_i} \overline{u_j}$ for momentum and $q_{ij} = \overline{u_i q_j} - \overline{u_i} \overline{q_j}$ for potential. Note that τ_{ij} expresses the effect of subgrid-scale motion on the resolved large scales and is often represented as an additional viscosity ν_t with the following formulation:

$$\tau_{ij} = -2\nu_t \overline{S}_{ij}, \quad (30)$$

where $\overline{S}_{ij} = \frac{1}{2} \left(\frac{\partial \overline{u}_i}{\partial x_j} + \frac{\partial \overline{u}_j}{\partial x_i} \right)$ is the strain rate tensor and ν_t the turbulent eddy viscosity. To determine the additional eddy viscosity, the standard Smagorinsky subgrid-scale model (Smagorinsky, 1963) is used:

$$\nu_t = (C_s \overline{\Delta})^2 |\overline{\mathbf{S}}|, \quad (31)$$

where $\overline{\Delta}$ is a length scale, C_s the Smagorinsky coefficient, and using the Einstein summation notation for standardization $|\overline{\mathbf{S}}| = \sqrt{2\overline{S}_{ij}\overline{S}_{ij}}$. The grid spacing is used as a measure for the length scale. This standard Smagorinsky subgrid-scale model is widely used in atmospheric and engineering applications. The Smagorinsky coefficient C_s has a theoretical value of about 0.2, as estimated by Lilly (1967). Applying this value to a turbulence-driven flow with thermal convection fields results in a good agreement with observations as shown by Deardorff (1972).

To take stratification effects into account, the standard Smagorinsky formulation is modified by changing the eddy viscosity to

$$\nu_t = (C_s \overline{\Delta})^2 \max \left[0, \left(|\overline{\mathbf{S}}|^2 \left(1 - \frac{Ri}{Pr} \right) \right)^{1/2} \right] \quad (32)$$

Title Page

Abstract

Introduction

Conclusions

References

Tables

Figures

◀

▶

◀

▶

Back

Close

Full Screen / Esc

Printer-friendly Version

Interactive Discussion



with

$$Ri = \frac{\frac{g}{\theta_p} \frac{\partial \theta_p}{\partial z}}{|\mathbf{S}|^2}. \quad (33)$$

Here Ri is the Richardson number and Pr is the turbulent Prandtl number. In a stable boundary layer the vertical gradient of the potential temperature is greater than zero (positive), which leads to a positive Richardson number and, thus, the additional term Ri/Pr reduces the square of the strain rate tensor and decreases the turbulent eddy viscosity. Therefore, less turbulent vertical mixing takes place.

The implementation in the ASAM code is accomplished in the main diffusion routine of the model. It develops the whole term of $\partial/\partial x_j [\rho D S_{ij}]$ for every time step. The coefficient D represents D_{mom} for the momentum and D_{pot} for the potential subgrid-scale stress. Further routines describe the computation of D_{mom} and D_{pot} the following way:

$$D_{\text{mom}} = (C_s \bar{\Delta})^2 |\mathbf{S}|. \quad (34)$$

The potential subgrid-scale stress is related to the Prandtl similarity and can be developed by dividing the subgrid-scale stress tensor for momentum by the turbulent Prandtl number Pr that typically has a value of $1/3$ (Deardorff, 1972). The length scale $\bar{\Delta}$ in the Standard Smagorinsky formulation is set to the value of grid spacing. However, the cut cell approach makes it difficult because of tiny and/or anisotrope cells. To overcome this deficit the value is defined after Scotti et al. (1993):

$$\bar{\Delta} = (\Delta_1 \Delta_2 \Delta_3)^{1/3} f(a_1, a_2). \quad (35)$$

Δ is the grid spacing in orthogonal directions, and a correction function f is applied as follows:

$$f(a_1, a_2) = \cosh \left[\frac{4}{27} \left(\ln^2 a_1 - \ln a_1 \ln a_2 + \ln^2 a_2 \right) \right]^{1/2}$$

4476

GMDD

7, 4463–4525, 2014

ASAM v2.7

M. Jähn et al.

Title Page

Abstract

Introduction

Conclusions

References

Tables

Figures

◀

▶

◀

▶

Back

Close

Full Screen / Esc

Printer-friendly Version

Interactive Discussion



$$\text{with } a_1 = \frac{\Delta_1}{\Delta_3}, \quad a_2 = \frac{\Delta_2}{\Delta_3}. \quad (36)$$

Here a_1 and a_2 are the ratios of grid spacing in different directions with the assumption, that $\Delta_1 \leq \Delta_2 \leq \Delta_3$. For an isotropic grid $f = 1$.

5 3.2 Two-moment warm cloud microphysics scheme

The implemented microphysics scheme is based on the work of Seifert and Beheng (2006). This scheme explicitly represents two moments (mass and number density) of the hydrometeor classes cloud droplets and rain drops. Ice phase hydrometeors are currently not implemented in the model. Altogether, seven microphysical processes are included: condensation/evaporation (“COND”), cloud condensation nuclei (CCN) activation to cloud droplets at supersaturated conditions (“ACT”), autoconversion (“AUTO”), self-collection of cloud droplets (“SCC”), self-collection of rain drops (“SCR”), accretion (“ACC”) and evaporation of rain (“EVAP”):

$$\frac{\partial(\rho q_v)}{\partial t} + \nabla \cdot (\rho \mathbf{v} q_v) = -S_{\text{COND}} - S_{\text{ACT}} + S_{\text{EVAP}}, \quad (37)$$

$$15 \quad \frac{\partial(\rho q_c)}{\partial t} + \nabla \cdot (\rho \mathbf{v} q_c) = +S_{\text{COND}} + S_{\text{ACT}} - S_{\text{AUTO}} - S_{\text{ACC}}, \quad (38)$$

$$\frac{\partial(\rho q_r)}{\partial t} + \nabla \cdot (\rho \mathbf{v} q_r) = +S_{\text{AUTO}} + S_{\text{ACC}} - S_{\text{EVAP}}, \quad (39)$$

$$\frac{\partial N_{\text{CCN}}}{\partial t} + \nabla \cdot (\mathbf{v} N_{\text{CCN}}) = -S_{\text{COND}_N} - S_{\text{ACT}_N} + S_{\text{EVAP}_N}, \quad (40)$$

$$\frac{\partial N_c}{\partial t} + \nabla \cdot (\mathbf{v} N_c) = +S_{\text{COND}_N} + S_{\text{ACT}_N} - S_{\text{AUTO}_N} - S_{\text{ACC}_N} - S_{\text{SCC}}, \quad (41)$$

$$20 \quad \frac{\partial N_r}{\partial t} + \nabla \cdot (\mathbf{v} N_r) = +S_{\text{AUTO}_N} + S_{\text{ACC}_N} - S_{\text{EVAP}_N} - S_{\text{SCR}}. \quad (42)$$

Details on the conversion rates can be found in Seifert and Beheng (2006). Additionally, a limiter function is used to ensure numerical stability and avoid non-physical negative values (Horn, 2012). Since there is no saturation adjustment technique in ASAM, the condensation process is taken as an example to demonstrate the physical meaning of the limiter functions. Considering the available water vapor density ρ_v and the cloud water density ρ_c , the process of condensation (or evaporation of cloud water, respectively) is forced by the water vapor density deficit and limited by the available cloud water.

$$\text{FOR} = \rho_v - (p_{vs}T/R_v) \quad (43)$$

$$\text{LIM} = \rho_c \quad (44)$$

$$S_{\text{COND}} = \frac{\text{FOR} - \text{LIM} + (\text{FOR}^2 + \text{LIM}^2)^{1/2}}{\tau_{\text{COND}}} \quad (45)$$

Here, p_{vs} is the saturation vapor pressure and the relaxation time is set to $\tau_{\text{COND}} = 1$ s. The numerator term is called Fischer–Burmeister function and has originally been used in optimization of complementary problems (cf. Kong et al., 2010). A simple model after Horn (2012) is applied to determine the corresponding changes in the number concentrations and to ensure a reduction of the cloud droplet number density to zero if there is no cloud water present. This means that N_c reduces when droplets are getting too small

$$S_{\text{COND}_N} = \min \left(0, C \left[\frac{\rho_c}{x_{\min}} - N_c \right] \right) \quad (46)$$

and increases when droplets are getting too large

$$S_{\text{COND}_N} = \max \left(0, C \left[\frac{\rho_c}{x_{\max}} - N_c \right] \right). \quad (47)$$

A time scale factor of $C = 0.01 \text{ s}^{-1}$ appears to be reasonable for this particular process.



3.3 Precipitation

The sedimentation velocity of raindrops is derived as in the operationally used COSMO model from the German Weather Service (Doms et al., 2011), There, the following assumptions are made. The precipitation particles are exponentially distributed with respect to their drop diameter (Marshall–Palmer distribution):

$$f_r(D) = N_0^r \exp -\lambda_r D \quad (48)$$

Here, λ_r is the slope parameter of the distribution function and $N_0^r = 8 \times 10^6 \text{ m}^{-4}$ is an empirically determined distribution parameter. The terminal fall velocity of raindrops is then assumed to be uniquely related to drop size, which is expressed by the following empirical function:

$$W_f(D) = c_r D^{1/2} \quad (49)$$

with $c_r = 130 \text{ m}^{1/2} \text{ s}^{-1}$. Finally, the precipitation flux of rainwater can be calculated by

$$\mathbf{P}_r = \rho_r W_f(\rho_r) = \int_0^{\infty} m(D) W_f(D) f_r(D) dD. \quad (50)$$

with the raindrop mass

$$m(D) = \pi \rho_W D^3 / 6, \quad (51)$$

where $\rho_W = 1000 \text{ kg m}^{-3}$ is the mass density of water. This leads to an expression for the terminal fall velocity of raindrops in dependence on their density:

$$W_f(\rho_r) = -c_r \frac{\Gamma(4,5)}{6} \left(\frac{\rho_r}{\pi \rho_W N_{0r}} \right)^{1/8}. \quad (52)$$

Title Page

Abstract

Introduction

Conclusions

References

Tables

Figures

◀

▶

◀

▶

Back

Close

Full Screen / Esc

Printer-friendly Version

Interactive Discussion



This takes place at the tendency equation for the rain water density:

$$\frac{\partial(\rho q_r)}{\partial t} + \nabla_h \cdot (\rho \mathbf{v}_h q_r) + \frac{\partial}{\partial z} (\rho q_r [w + W_f]) = S_{q_r}. \quad (53)$$

3.4 Surface fluxes

- 5 A simple way to parameterize surface heat fluxes is the usage of a constant flux layer. There, the energy flux is directly given and does not depend on other variables. With the density potential temperature formulation (Eq. 3), the source term for this quantity has to be calculated:

$$\begin{aligned} \frac{\partial(\rho \theta_\rho)}{\partial t} + \frac{\partial}{\partial x_j} (\rho \theta_\rho u_j) &= \rho \frac{\partial \theta_\rho}{\partial t} + \theta_\rho \frac{\partial \rho}{\partial t} + \theta_\rho \frac{\partial \rho u_j}{\partial x_j} + \rho u_j \frac{\partial \theta_\rho}{\partial x_j} \\ &= \rho \left(\frac{\partial \theta_\rho}{\partial t} + u_j \frac{\partial \theta_\rho}{\partial x_j} \right) + \theta_\rho \left(\frac{\partial \rho}{\partial t} + \frac{\partial \rho u_j}{\partial x_j} \right) \\ &= \rho \frac{d\theta_\rho}{dt} + \theta_\rho S_v. \end{aligned} \quad (54)$$

S_v is the source term of water vapor in units of $[\text{kg m}^{-3} \text{ s}^{-1}]$. Considering Eq. (A33), adding the sensible heat flux and neglecting phase changes leads to

$$15 \quad \frac{\partial(\rho \theta_\rho)}{\partial t} + \frac{\partial}{\partial x_j} (\rho \theta_\rho u_j) = S_{\theta_\rho} \quad (55)$$

with

$$S_{\theta_\rho} = \rho \theta_\rho \left(\frac{S_h}{T} + \frac{S_v}{\rho_d} \left[\frac{R_v}{R_m} - \ln \pi \left(\frac{R_v}{R_m} - \frac{c_{pv}}{c_{pml}} \right) \right] \right) \quad (56)$$

where S_h is the heat source in units of $[Ks^{-1}]$, $R_m = R_d + r_v R_v$ and $c_{pml} = c_{pd} + r_v c_{pv} + r_l c_{pl}$ are the gas constant and the specific heat capacity for the air mixture, respectively.

The corresponding surface fluxes in $[W m^{-2}]$ are:

$$S_{sens} = S_h \frac{\rho_d c_{pml}}{\rho A}, \quad (57)$$

$$S_{lat} = S_v L_v(T) \frac{V}{A}. \quad (58)$$

Here, $L_v = L_{00} + (c_{pv} - c_{pl})T$ is the latent heat of vaporization, A is the cell surface at the bottom boundary and V the cell volume.

For the computation of the surface fluxes around cut cells, an interpolation technique is used:

$$\frac{\partial(\rho\theta_\rho)}{\partial t} + \frac{\partial}{\partial x_j}(\rho\theta_\rho u_j) = S_{\theta_\rho} \min\left(\frac{V}{V_{max}}, 1\right) \quad (59)$$

with the maximum cell volume $V_{max} = \Delta x \Delta y \Delta z$. For surrounding cells, the missing flux fraction is distributed depending on the left and right cut faces A^L and A^R in all spatial directions:

$$\frac{\partial(\rho\theta_\rho)}{\partial t} + \frac{\partial}{\partial x_j^L}(\rho\theta_\rho u_j^L) = S_{\theta_\rho} \frac{\max\left(\frac{A_j^L - A_j^R}{V_{max}, 0}\right) V_{max} - V}{A_{surf} V_{max}}, \quad (60)$$

$$\frac{\partial(\rho\theta_\rho)}{\partial t} + \frac{\partial}{\partial x_j^R}(\rho\theta_\rho u_j^R) = S_{\theta_\rho} \frac{\max\left(\frac{A_j^R - A_j^L}{V_{max}, 0}\right) V_{max} - V}{A_{surf} V_{max}}, \quad (61)$$

where the superscripts L and R correspond to the left and right neighbor cell, respectively. The total surface is computed by

$$A_{surf} = \sum |A_j^L - A_j^R|. \quad (62)$$



3.5 Soil model

In order to account for the interaction between land and atmosphere and the high diurnal variability of the meteorological variables in the surface layer, a soil model has been implemented into ASAM. In contrast to the constant flux layer model, the computation of the heat and moisture fluxes are now dependent on radiation, evaporation and the transpiration of vegetated area. Phase changes are not covered yet and intercepted water is only considered in liquid state.

Two different surface flux schemes are implemented, following the revised Louis scheme as integrated in the COSMO model (Doms et al., 2011) and the revised flux scheme as used in the WRF model (Jiménez et al., 2012). The surface fluxes of momentum, heat and moisture are parameterized in the following way, respectively:

$$\tau_{zx} = \rho C_m |\mathbf{v}_h| u(h), \quad (63a)$$

$$-\rho c_p \overline{w'\theta'} = \rho c_p C_h |\mathbf{v}_h| (\theta(h) - \theta(z_{0T})), \quad (63b)$$

$$-\rho L \overline{w'q'} = \rho L C_q |\mathbf{v}_h| (q(h) - q(z_{0q})). \quad (63c)$$

C_m , C_h and C_q are the bulk transfer coefficients and it is considered that $C_h = C_q$. As described in (Doms et al., 2011), the bulk transfer coefficients are defined as the product of the transfer coefficients under neutral conditions $C_{m,h}^n$ and the stability functions $F_{m,h}$ depending on the Bulk-Richardson-Number Ri_B and roughness length z_0 .

$$C_{m,h} = C_{m,h}^n F_{m,h}(Ri_B, z/z_0). \quad (64)$$

In Jiménez et al. (2012) the bulk transfer coefficients are defined as follows

$$C_{m,h} = \frac{k^2}{\Psi_M \Psi_{M,H}} \quad (65)$$

with

$$\Psi_{M,H} = \ln\left(\frac{z+z_0}{z_0}\right) - \phi_{m,h}\left(\frac{z+z_0}{L}\right) + \phi_{m,h}\left(\frac{z_0}{L}\right) \quad (66)$$

Title Page

Abstract

Introduction

Conclusions

References

Tables

Figures

◀

▶

◀

▶

Back

Close

Full Screen / Esc

Printer-friendly Version

Interactive Discussion



and $\phi_{m, h}$ representing the integrated similarity functions. L stands for the Obukhov length and k is the von-Kármán-constant. In neutral to highly stable conditions $\phi_{m, h}$ follows Cheng and Brutsaert (2005) and in unstable situations the ϕ -functions follow Fairall et al. (1996). For further details concerning limitations and restrictions see Jiménez et al. (2012). Test cases for validation indicate that the surface fluxes are better reproduced by Jiménez et al. (2012) than for Doms et al. (2011).

The transport of the soil water as a result of hydraulic pressure due to diffusion and gravity within the soil layers is described by Richard's equation:

$$\frac{\partial W_{\text{soil},k}}{\partial t} = \frac{\partial}{\partial z} \left(D_{\text{diff}} \frac{\partial W_{\text{soil},k}}{\partial z} + \kappa_{\text{soil},k} \right) \quad (67)$$

with the diffusion coefficient

$$D_{\text{diff}} = \kappa_{\text{soil},k} \frac{\partial \Psi_{\text{soil},k}}{\partial W_{\text{soil},k}}. \quad (68)$$

$W_{\text{soil},k}$ is the volumetric water content in the k th soil layer. Ψ_{soil} stands for the matric potential and κ_{soil} is the hydraulic conductivity. Ψ_{soil} and κ_{soil} are parameterized based on Van Genuchten (1980):

$$\kappa_{\text{soil}} = \kappa_{\text{sat}} \sqrt{W_{\text{eff}}} \left(1 - \left[1 - (W_{\text{eff}})^{\frac{1}{m}} \right]^m \right)^2 \quad (69)$$

$$\Psi_{\text{soil}} = \Psi_{\text{sat}} \left[(W_{\text{eff}})^{-\frac{1}{m}} - 1 \right]^{\frac{1}{n}} \quad (70)$$

W_{eff} describes the effective soil wetness, which takes a residual water content W_{res} into account, restricting the soil from complete desiccation. κ_{sat} and Ψ_{sat} are the hydraulic conductivity and the matric potential at saturated conditions, respectively. The parameters m and n describe the pore distribution (Braun, 2002) with $m = 1 - 1/n$ (also see Tables B1 and B2).



[Title Page](#)[Abstract](#)[Introduction](#)[Conclusions](#)[References](#)[Tables](#)[Figures](#)[◀](#)[▶](#)[◀](#)[▶](#)[Back](#)[Close](#)[Full Screen / Esc](#)[Printer-friendly Version](#)[Interactive Discussion](#)

Further addition/extraction of soil water is controlled by the percolation of intercepted water into the ground and the evaporation and transpiration of water from bare soil and vegetation. The mechanisms implemented are based on the Multi-Layer Soil and Vegetation Model TERRA_ML as described in Doms et al. (2011). The evaporation of bare soil is adjusted to the parameterization proposed by Noilhan and Planton (1989). It is defined as the difference between the specific humidity q_{air} and the surface saturation humidity $q_{\text{sat}}(T_{\text{sfc}})$ in dependence of the soil water content $W_{\text{soil},1}$ and the field capacity W_{fc} , which is expressed by the near-surface relative humidity h_{u} . The evaporation of bare soil writes as

$$E_{\text{bare}} = (1 - f_{\text{plant}}) \rho_{\text{air}} L_{\text{v}} C_{\text{h}} |v_{\text{h}}| (h_{\text{u}} q_{\text{sat}}(T_{\text{sfc}}) - q_{\text{air}}) \quad (71)$$

with

$$h_{\text{u}} = \begin{cases} 0.5 \left[1 - \cos \left(\frac{\pi}{1.6} \frac{W_{\text{soil},1}}{W_{\text{fc}}} \right) \right], & \text{if } W_{\text{soil},1} < W_{\text{fc}} \\ 1.0, & \text{if } W_{\text{soil},1} \geq W_{\text{fc}} \end{cases} \quad (72)$$

and f_{plant} being the seasonally quantified vegetation cover based on Braun (2002) and L_{v} standing for the latent heat of vaporization. For $(q_{\text{sat}}(T_{\text{surf}}) \geq q_{\text{air}})$ and $(h_{\text{u}} q_{\text{sat}}(T_{\text{surf}}) - q_{\text{air}}) \leq 0$, $E_{\text{bare}} = 0$.

The variation of the soil temperature is a result of heat conductivity depending on the soil texture and the soil water content of the respective soil layer:

$$\frac{\partial T_{\text{soil}}}{\partial t} = \frac{1}{\rho c} \frac{\partial}{\partial z} \left[\lambda \frac{\partial T_{\text{soil}}}{\partial z} + E_{\text{q}} \rho_{\text{w}} c_{\text{w}} \bar{T}_{\text{soil}} \right] \quad (73)$$

T_{soil} is the absolute temperature in the k th soil layer in [K], \bar{T}_{soil} is the mean soil temperature of two neighboring soil layers. The change in internal energy due to changes in moisture by the inner soil water flux, evapotranspiration and evaporation from the upper soil layer and the interception reservoir is treated by the second term in square

brackets. The heat conductivity λ and the volumetric heat capacity ρc are variables that depend on the soil texture. The heat capacity of the soil ρc formulated by Chen and Dudhia (2001) is the sum of the heat capacity of dry soil ($\rho_0 c_0$, see Tables B1 and B2), the heat capacity of wet soil ($\rho_w c_w$) and the heat capacity of the air within the soil pores ($\rho_a c_a$).

$$\rho c = W_{\text{soil}} \rho_w c_w + (1 - W_{\text{pv}}) \rho_0 c_0 + (W_{\text{pv}} - W_{\text{soil}}) \rho_a c_a \quad (74)$$

with W_{pv} corresponding to the soil pores and $\rho_w c_w = 4.18 \times 10^6 \text{ J m}^{-3} \text{ K}^{-1}$ and $\rho_a c_a = 1298 \text{ J m}^{-3} \text{ K}^{-1}$. The heat conductivity λ is defined after Pielke (1984):

$$\lambda = \begin{cases} 418 \exp\{-\Psi_{\log} - 2.7\} & \text{if } \Psi_{\log} \leq 5.1 \\ 0.172 & \text{if } \Psi_{\log} > 5.1 \end{cases} \quad (75)$$

with $\Psi_{\log} = \log_{10}|100\Psi_{\text{soil}}|$.

The topmost layer is exposed to the incoming radiation and thus has the strongest variation in temperature in comparison to the other soil layers within the ground. The temperature equation of the first layer is, in addition to the incoming radiation, determined by the latent and sensible heat flux.

$$\frac{\partial T_{\text{soil},1}}{\partial t} = \frac{1}{\rho c} \frac{\partial}{\partial z} \left[\left(\lambda \frac{\partial T_{\text{soil},1}}{\partial z} \right) + \Delta Q \right] \quad (76)$$

with

$$\Delta Q = Q_{\text{dir}} + Q_{\text{dif}} - \sigma T_{\text{sfc}}^4 - c_p Q_{\text{SH}} - L_v Q_{\text{LH}} \quad (77)$$

Here Q_{LH} is the latent heat flux, describing the moisture flux between soil and atmosphere as the sum of evaporation and transpiration and Q_{SH} is the sensible heat flux. Q_{dir} and Q_{dif} represents the direct and diffusive irradiation, respectively.

4 Test cases

In this section, we present three example test cases, which show that the model produces reasonable results when comparing them with standard benchmarks. The first case is a sinking cold bubble in a dry environment, from which a density current develops (Straka et al., 1993). Considering moisture effects, the moist bubble case by Bryan and Fritsch (2002) is performed. A 2-D gravity wave test case around an idealized mountain range (Schäfer et al., 2002) is simulated to demonstrate the ability of the model to resolve the flow around orography by using the cut cell approach.

4.1 Cold bubble

A first non-linear test problem is the density current simulation study documented in Straka et al. (1993). In this case, the computational domain extends from -25.6 to 25.6 km in horizontal direction and from 0 to 6.4 km in vertical direction with isotropic grid spacing of $\Delta x = \Delta z = 50$ m. The total integration time is $t = 1800$ s. The initial atmosphere is a dry and hydrostatically balanced state. A fixed physical viscosity is used with $\nu = 75 \text{ m}^2 \text{ s}^{-1}$ and there is a horizontally homogeneous environment with $\bar{\theta} = 300$ K. The perturbation (cold bubble with negative buoyancy) is defined by

$$T = \begin{cases} 0.0^\circ\text{C} & \text{if } L > 1.0, \\ -15.0^\circ\text{C}(\cos[\pi L] + 1.0)/2. & \text{if } L \leq 1.0 \end{cases} \quad (78)$$

where

$$L = \left(\left[(x - x_c)x_r^{-1} \right]^2 + \left[(z - z_c)z_r^{-1} \right]^2 \right)^{0.5} \quad (79)$$

and $x_c = 0.0$ km, $x_r = 4.0$ km, $z_c = 3.0$ km and $z_r = 2.0$ km. The temporal evolution for this density current test case is shown in Fig. 5. After 900 s integration time, the flow field has spread up to $x \approx 16$ km, which corresponds to maximum horizontal wind



speeds of $u_{\max} = 37 \text{ m s}^{-1}$. These values and the contour field agree well with the results from the literature.

4.2 Moist bubble

The moist bubble benchmark case after Bryan and Fritsch (2002) is based on its dry counterpart described in Wicker and Skamarock (1998). There, a hydrostatic and neutrally balanced initial state is realized by a constant potential temperature. A warm perturbation in the center of the domain leads to the rising thermal. For the present test case, a moist neutral state can be expressed with the equivalent potential temperature θ_e and two assumptions: the total water mixing ratio $r_t = r_v + r_l$ remains constant and phase changes between water vapor and liquid water are exactly reversible. The perturbation field takes the following form:

$$\theta' = 2 \cos^2 \left(\frac{\pi L}{2} \right) \quad (80)$$

with

$$L = \sqrt{\left(\frac{x - x_c}{x_r} \right)^2 + \left(\frac{z - z_c}{z_r} \right)^2} \quad (81)$$

The parameters $x_c = 10 \text{ km}$, $z_c = 2 \text{ km}$ and $x_r = z_r = 2 \text{ km}$ determine the position and radius of the moist heat bubble. The domain is 20 km long in x direction and the vertical extend is 10 km . Grid spacing is again isotropic with $\Delta x = \Delta z = 100 \text{ m}$. In addition to the original test case, a uniform horizontal velocity of $U = 20 \text{ m s}^{-1}$ is applied. With that, the center of the bubble is again located at $x = 0 \text{ m}$ at $t = 1000 \text{ s}$ after passing through the periodic boundaries. The position of the rising thermal is shown in Fig. 6. These results are in very good agreement with the ones from the benchmark. In our case, there is a slight asymmetry at the top of the thermal due to the lateral transport. Because of the fully compressible design in ASAM, mass conservation is always

Title Page

Abstract

Introduction

Conclusions

References

Tables

Figures

◀

▶

◀

▶

Back

Close

Full Screen / Esc

Printer-friendly Version

Interactive Discussion



ensured. Energy is not fully conserved, but the total relative energy error stays in an acceptable range of 10^{-4} % when the top of the thermal reaches its height of 8 km. After Bryan and Fritsch (2002), both mass and energy conservation are required to obtain the benchmark result.

4.3 2-D mountain gravity waves

In this test case, a flow over a mountain ridge is simulated (Schaer et al., 2002). A dry stable atmosphere is defined by a constant Brunt–Väisälä frequency of $N = 0.01 \text{ s}^{-1}$ and $\theta_0 = 300 \text{ K}$. A uniform horizontal wind speed of $U = 10 \text{ m s}^{-1}$ is applied. The domain extends 200 km horizontally and 19.5 km vertically with grid spacings of $\Delta x = 500 \text{ m}$ and $\Delta z = 300 \text{ m}$. The structure of the mountain ridge is represented by a bell curve shape with superposed variations:

$$h(x) = h_0 \exp\left(-[x/a]^2\right) \cos^2\left(\pi x/\lambda\right) \quad (82)$$

with $h_0 = 250 \text{ m}$, $a = 5 \text{ km}$ and $\lambda = 4 \text{ km}$. The simulation result for the steady state is shown in Fig. 7. There are no non-physical distorted wave patterns and the result agrees very well with the analytical solution shown in Schaer et al. (2002).

5 Application for real case experiments: Barbados sensitivity study

For the following sensitivity study, four model runs are performed on a $110 \text{ km} \times 110 \text{ km} \times 6 \text{ km}$ domain with $256 \times 256 \times 38$ grid points and inflow/outflow lateral boundary conditions. The vertical spacing is finer at lower levels to better represent the orographical structure and to resolve boundary layer dynamics more accurately. The topographic data with a 100 m resolution is obtained from the Consortium for Spatial Information (CGIAR-CSI) Shuttle Radar Topography Mission (SRTM) dataset (<http://srtm.csi.cgiar.org>). The Coriolis parameter $f = 3.3 \times 10^{-5} \text{ s}^{-1}$ is calculated from a latitude value of



$\phi = 13.18^\circ$ N. Total integration time is 24 h for all simulations, starting at midnight. An overview about the LES model configuration is given in Table 4.

Idealized initial profiles are used with respect to hydrostatic equilibrium with positive Brunt–Väisälä-Frequency $N_d = 11 \times 10^{-3} \text{ s}^{-1}$, ground values of potential temperature $\theta_0 = 298.15 \text{ K}$ and air pressure $p_0 = 1000 \text{ hPa}$. To represent an inversion layer, the relative humidity profile is linearly increasing up to a height of 1500 m. At this level, there is a strong decrease down to half of its initial value and then it is slowly increasing again. A logarithmic wind profile up to $z_L = 300 \text{ m}$ is applied to take roughness effects into account. Above this level, there is a uniform flow.

$$u(z) = \begin{cases} u_0 \frac{\log(z/z_0)}{\log(z_L/z_0)} & \text{if } z < z_L \\ u_0 & \text{if } z \geq z_L. \end{cases} \quad (83)$$

The surface roughness is set to a value of $z_0 = 0.0002 \text{ m}$ for the ocean and $z_0 = 0.5 \text{ m}$ for the island.

To parameterize the ocean and island surface fluxes, values have been taken from a complementary Doppler lidar and LES study of island effects for Cape Verde islands (Engelmann et al., 2011). Since both Cape Verde and Barbados are located at roughly the same latitude, this approach appears to be reasonable in the framework of this sensitivity study. Figure 8 shows the diurnal variation of the sensible heat flux over Barbados as it is parameterized in the model. The underlying cosine function takes to following form:

$$Q_s(t) = \hat{Q}_s \cos\left(\frac{t - t_{Q_{\max}}}{t_{\text{day}}/\pi}\right) + Q_{\min}, \quad (84)$$

where in our case $\hat{Q}_s = 600 \text{ W m}^{-2}$ and the radiative cooling factor $Q_{\min} = -77 \text{ W m}^{-2}$. This leads to a maximum sensible heat flux of 523 W m^{-2} . The parameter $t_{Q_{\max}}$ is the time of day where the maximum value of the surface sensible heat flux is reached and



[Title Page](#)[Abstract](#)[Introduction](#)[Conclusions](#)[References](#)[Tables](#)[Figures](#)[Back](#)[Close](#)[Full Screen / Esc](#)[Printer-friendly Version](#)[Interactive Discussion](#)

t_{day} is the time span between sunrise and sunset. Here, the chosen values represent a mid-July day with $t_{Q_{\text{max}}} = 13$ h and $t_{\text{day}} = 12.84$ h. Diurnal variations of the latent heat flux are not taken into account. It remains constant with a value of $Q_l = 55 \text{ W m}^{-2}$. The maritime surface fluxes are set to 20 W m^{-2} and 90 W m^{-2} for sensible and latent heat flux, respectively. To break the model symmetry and support the generation of a maritime boundary layer, a random noise of $\pm 0.5 \text{ W m}^{-2}$ is imposed on the latent heat fluxes.

Different simulation cases are performed to study the model sensitivity on different parameters (Table 5). The reference case (REF) is characterized by an easterly flow with a wind velocity of $U = 10 \text{ m s}^{-1}$, which is a typical value for the Caribbean trade wind region. The relative humidity at the ground is set to $\text{RH}_0 = 70\%$. To study the influence of topographical effects, the island orography is removed in the FLAT case. The sensitivity of the large-scale dynamical forcing is tested in the U05 case, where the mean wind speed is halved compared to the reference case. For the last simulation case, the initial moisture load is changed. There, the ground relative humidity value is set to 80% (RH80 case). The 10% increase up to the inversion height remains unchanged.

Since the REF case reflects a typical meteorological situation for a summer day at Barbados, we will begin the analysis with this case. Figure 9 shows the vertical velocity field together with potential temperature isolines in 400 m height above sea level at 14:00 LT. A persistent up- and downwind pattern over the island is caused by the orography displayed in Fig. 10. The L-shaped hill pattern leads to upwinds at the north-eastern part of Barbados, whereas in the west there are mainly descent flows. Quantitatively, the vertical velocity field at 400 m height is modified by $\pm 1 \text{ m s}^{-1}$. One may also see that the vertical wind field is perturbed by small convection cells. Nevertheless, topographical forces dominate the vertical velocity field w in the case of non-weak horizontal winds. Since gravity waves propagate in every spatial direction, a coniform wave structure forms west of Barbados.

[Title Page](#)[Abstract](#)[Introduction](#)[Conclusions](#)[References](#)[Tables](#)[Figures](#)[◀](#)[▶](#)[◀](#)[▶](#)[Back](#)[Close](#)[Full Screen / Esc](#)[Printer-friendly Version](#)[Interactive Discussion](#)

Looking at the FLAT case (Fig. 11), where all island elevations are removed, the flow field over the island is mainly characterized by small convective cells, which are stronger than in the REF case. This is the case because there are no predominant downdrafts caused by orography at the western part of the island. Thus, there is no suppression of convection there. Here, the updrafts are alongside a latitude line where the largest landmass area is overflowed, which is at least 5 km farther south.

Due to the strong horizontal winds and comparably low relative humidity, there is no cloud generation during the whole simulation time in the REF and FLAT cases. However, if the mean wind speed is lowered or the moisture load is increased (U05, RH80), shallow cumulus clouds form in the vicinity of the island. Figure 12 shows the diurnal variation of the total cloud cover for the cases where clouds are simulated. Due to the radiative cooling during the night (parameterized by negative sensible heat flux) over the island, a bit of fog develops in the lowest layer between 02:00 and 07:00 LT at the U05 case. This does not appear at the RH80 case because there is a faster mixing of warm maritime air that is advected toward the island area. During the afternoon hours, island-induced cumulus clouds develop, which leads to an at least 3 times higher cloud coverage at RH80 compared to U05. In both cases, the maximum cloud cover is reached around 14:00 LT. Figure 13 shows the domain-averaged integrated water paths for the RH80 case. As one can see, these clouds also produce some drizzle with maximum values of the mean rain water path of about 0.05 g m^{-2} at 13:00 LT.

Shallow cumulus clouds are most likely located along the updraft line westward of the island (e.g. in Fig. 9). The position of this line is similar to the REF case. A snapshot of a modeled cloud street is shown in Fig. 14. The base height of these clouds is at 800–900 m a.s.l. They are basically formed due to a modification of the temperature and humidity field by the island surface roughness and increased heat capacity. Both effects are taken into account within the LES model by the logarithmic wind profile (dependent on roughness height) and the constant flux layer with diurnal variation of the sensible heat flux over the island area. Cloud streets are frequently observed every 2–3 days during afternoon hours if there is no large-scale synoptical disturbance.

[Title Page](#)[Abstract](#)[Introduction](#)[Conclusions](#)[References](#)[Tables](#)[Figures](#)[⏪](#)[⏩](#)[◀](#)[▶](#)[Back](#)[Close](#)[Full Screen / Esc](#)[Printer-friendly Version](#)[Interactive Discussion](#)

The performed simulations show that the model is capable to resolve boundary layer dynamics around the island as well as island-induced shallow cumulus cloud street generation. Considering numerical sensitivity studies on island effects by Savijärvi and Matthews (2004), the general conclusion is that forced rising and sinking motions and their consecutive effects can only be explained if island orography is accurately included in the numerical models, which is a particular feature in ASAM. Topographically forced components will dominate if the large-scale mean wind is in the order of magnitude of about 10 m s^{-1} , which is the case for Barbados.

The model will contribute to further studies in the Carribean trade wind area, e.g. for the SALTRACE (Saharan Aerosol Long-range Transport and Aerosol–Cloud-Interaction Experiment, <http://www.pa.op.dlr.de/saltrace/>) campaign at Barbados. Initial profiles will be taken from radiosonde or drop sonde data. For those upcoming numerical studies, the soil model described in Sect. 3.5 will replace the constant flux layer approach to get a more accurate representation of vertical surface fluxes. Measurement data from wind or depolarization lidar can be used to validate model results. Furthermore, simulation data can serve to fill the gap caused by missing measurement series, e.g. time-resolved vertical profiles of humidity and temperature during the day, which are difficult to obtain from lidar systems.

6 Conclusions and future work

A detailed description of the fully compressible, nonhydrostatic All Scale Atmospheric Model (ASAM) was presented. Since the cut cell method is used within a Cartesian grid, the concept of the spatial discretization as well as an implicit Rosenbrock time integration scheme with splitting of the Jacobian were outlined. Sophisticated physical parameterizations (Smagorinsky subgrid scale model, two-moment warm microphysics scheme, multilayer soil model), which find application in different existing models, are implemented in ASAM. A special technique to interpolate the surface heat fluxes with respect to the irregular grid around cut cells was described. The model produces very

[Title Page](#)[Abstract](#)[Introduction](#)[Conclusions](#)[References](#)[Tables](#)[Figures](#)[⏪](#)[⏩](#)[◀](#)[▶](#)[Back](#)[Close](#)[Full Screen / Esc](#)[Printer-friendly Version](#)[Interactive Discussion](#)

good results for typical benchmark test cases from the literature. It is also shown that it is possible to perform three-dimensional large eddy simulations for an island-ocean system including island topography. The convective boundary layer over the island during the day is well resolved and also the development of shallow cumulus cloud streets can be simulated, which is in good agreement with observations. Model results will be used to contribute to upcoming measurements from field campaigns.

The focus on future model development lies on different aspects. Firstly, for the description of turbulence, other (dynamic) Smagorinsky models (e.g. Kleissl et al., 2006; Porté-Agel et al., 2000) might be better suited for particular simulations compared to the present model version. Also, a so-called implicit LES will be tested and verified. There, no turbulence model is used and the numerics of the discretization generate unresolved turbulent motions themselves. In this type of LES, the sensitivity of the thermodynamical formulation (especially in the energy equation) on the resulting motions has to be analyzed. Performance tests for highly parallel computing with a large number of processors will be conducted. Furthermore, high-frequency output is desired for statistical data analysis. For this reason, efficient techniques like adaption of the output on modern parallel visualization software will be developed.

Appendix A: Derivation of tendency equations

In this section, a straightforward derivation of the density potential temperature tendency equation is given to get the necessary source terms for microphysics, surface fluxes and precipitation. Therefore, phase changes are allowed and a water vapor source term S_v and sedimentation velocity W_f for rain drops are added to the system.

$$\frac{d\rho}{dt} = -\rho\nabla\cdot\mathbf{v} + S_v - S_{\text{fall}}, \quad (\text{A1})$$

$$\frac{d\rho_v}{dt} = -\rho_v\nabla\cdot\mathbf{v} + S_v + S_{\text{ph}}, \quad (\text{A2})$$

$$\frac{d\rho_l}{dt} = -\rho_c \nabla \cdot \mathbf{v} - S_{\text{ph}} - S_{\text{fall}}, \quad (\text{A3})$$

$$\frac{d\rho_d}{dt} = -\rho_d \nabla \cdot \mathbf{v}. \quad (\text{A4})$$

The precipitation term is $S_{\text{fall}} = \partial/\partial z(\rho_r W_f)$ with the sedimentation velocity W_f after Eq. (52). One can rewrite the Eqs. (A2) and (A3) with the mixing ratios $r_v = \rho_v/\rho_d$ and $r_l = \rho_l/\rho_d$:

$$\frac{dr_v}{dt} = \frac{1}{\rho_d}(S_v + S_{\text{ph}}), \quad (\text{A5})$$

$$\frac{dr_l}{dt} = -\frac{1}{\rho_d}(S_{\text{ph}} + S_{\text{fall}}). \quad (\text{A6})$$

For the sake of simplicity (regarding the following derivations) the liquid water density and mixing ratio are used with $\rho_l = \rho_c + \rho_r$ or $r_l = r_c + r_r$. The model however solves the prognostic equations for the cloud water density ρ_c and rain water density ρ_r separately.

A1 Internal energy and absolute temperature

A prognostic equation for the internal energy e is derived from the first law of thermodynamics, cf. Bott (2008, Eq. 31) and Satoh et al. (2008, Eq. B.13):

$$\frac{\partial(\rho e)}{\partial t} + \nabla \cdot (\rho e \mathbf{v}) = -\rho \nabla \cdot \mathbf{v} + S_e - \frac{\partial}{\partial z}(\rho_r W_f e_l) - \rho_r W_f g, \quad (\text{A7})$$

and alternatively with the specific enthalpy h in the advection part:

$$\frac{\partial(\rho e)}{\partial t} + \nabla \cdot (\rho h \mathbf{v}) = \mathbf{v} \cdot \nabla \rho + S_e - \frac{\partial}{\partial z}(\rho_r W_f e_l) - \rho_r W_f g. \quad (\text{A8})$$

There, the total specific internal energy is

$$e = h - \frac{p}{\rho} = (q_d c_{\text{vd}} + q_v c_{\text{vv}} + q_l c_{\text{pl}})T + q_v L_{00}, \quad (\text{A9})$$

Title Page

Abstract

Introduction

Conclusions

References

Tables

Figures

◀

▶

◀

▶

Back

Close

Full Screen / Esc

Printer-friendly Version

Interactive Discussion



and the specific internal energy for liquid water

$$e_l = h_l = c_{pl}T. \quad (\text{A10})$$

5 The term S_e is related to the water vapor source term:

$$S_e = h_v S_v. \quad (\text{A11})$$

Transforming Eq. (A7) into a tendency equation for the absolute temperature:

$$e \left(\frac{\partial \rho}{\partial t} + \nabla \cdot (\rho \mathbf{v}) \right) + \rho \left(\frac{\partial e}{\partial t} + \mathbf{v} \cdot \nabla e \right) = \text{RHS(A7)}$$

$$10 \quad e(S_v - S_{\text{fall}}) + \rho \frac{de}{dt} = \text{RHS(A7)}$$

$$e(S_v - S_{\text{fall}}) + \frac{d(\rho e)}{dt} - e \frac{d\rho}{dt} = \text{RHS(A7)} \quad (\text{A12})$$

With Eq. (A9), this leads to

$$\begin{aligned} \frac{d(\rho e)}{dt} &= \frac{d}{dt} ([\rho_d c_{vd} + \rho_v c_{vv} + \rho_l c_{pl}]T + \rho_v L_{00}) \\ 15 \quad &= T \left(c_{vd} \frac{d\rho_d}{dt} + c_{vv} \frac{d\rho_v}{dt} + c_{pl} \frac{d\rho_l}{dt} \right) + (\rho_d c_{vd} + \rho_v c_{vv} + \rho_l c_{pl}) \frac{dT}{dt} + L_{00} \frac{d\rho_v}{dt} \\ &\quad - (\rho_d c_{vd} + \rho_v c_{vv} + \rho_l c_{pl}) T \nabla \cdot \mathbf{v} + T c_{vv} (S_v + S_{\text{ph}}) - T c_{pl} (S_{\text{ph}} + S_{\text{fall}}) \\ &\quad + (\rho_d c_{vd} + \rho_v c_{vv} + \rho_l c_{pl}) \frac{dT}{dt} - L_{00} (\rho_v \nabla \cdot \mathbf{v} - S_v - S_{\text{ph}}) \\ &= -e \rho \nabla \cdot \mathbf{v} + (\rho_d c_{vd} + \rho_v c_{vv} + \rho_l c_{pl}) \frac{dT}{dt} + T (c_{vv} [S_v + S_{\text{ph}}] - c_{pl} [S_{\text{ph}} + S_{\text{fall}}]) \\ &\quad + L_{00} (S_v + S_{\text{ph}}), \end{aligned} \quad (\text{A13})$$

$$e \frac{d\rho}{dt} = e(S_v - S_{\text{fall}}) - e\rho\nabla \cdot \mathbf{v}. \quad (\text{A14})$$

Inserting Eqs. (A13) and (A14) in Eq. (A12):

$$\begin{aligned} \rho_d c_{\text{vml}} \frac{dT}{dt} &= -T(c_{\text{vv}}[S_v + S_{\text{ph}}] - c_{\text{pl}}[S_{\text{ph}} + S_{\text{fall}}]) - L_{00}(S_v + S_{\text{ph}}) - \rho\nabla \cdot \mathbf{v} + S_v h_v \\ &\quad - \frac{\partial}{\partial z}(\rho_r W_f e_l) - \rho_r W_f g \\ &= -\rho\nabla \cdot \mathbf{v} + (h_v - c_{\text{vv}}T - L_{00})S_v + (c_{\text{pl}}T - c_{\text{vv}}T - L_{00})S_{\text{ph}} \\ &\quad - \frac{\partial}{\partial z}(\rho_r W_f e_l) - \rho_r W_f g. \end{aligned} \quad (\text{A15})$$

Here we define

$$c_{\text{vml}} \equiv c_{\text{vd}} + r_v c_{\text{vv}} + r_l c_{\text{pl}}. \quad (\text{A16})$$

Rewriting the pressure and elimination of the velocity divergence:

$$-\rho\nabla \cdot \mathbf{v} = -(\rho_d R_d + \rho_v R_v)T \left(-\frac{1}{\rho_d} \frac{d\rho_d}{dt} \right) = (R_d + r_v R_v)T \frac{d\rho_d}{dt}, \quad (\text{A17})$$

$$\begin{aligned} \frac{d\rho_d}{dt} &= \frac{1}{R_d T \left(1 + \frac{r_v}{\varepsilon}\right)} \frac{d\rho}{dt} - \frac{\rho R_d T}{\varepsilon \left(R_d T \left[1 + \frac{r_v}{\varepsilon}\right]\right)^2} \frac{dr_v}{dt} - \frac{\rho}{R_d T^2 \left(1 + \frac{r_v}{\varepsilon}\right)} \frac{dT}{dt} \\ &= \frac{\rho_d}{\rho} \frac{d\rho}{dt} - \frac{\rho_d}{\varepsilon + r_v} \frac{dr_v}{dt} - \frac{\rho_d}{T} \frac{dT}{dt} \end{aligned} \quad (\text{A18})$$

$$\begin{aligned} \Rightarrow -\rho\nabla \cdot \mathbf{v} &= \frac{d\rho}{dt} - \rho_d R_v T \frac{dr_v}{dt} - (\rho_d R_d + \rho_v R_v) \frac{dT}{dt} \\ &= \frac{d\rho}{dt} - R_v T(S_v + S_{\text{ph}}) - (\rho_d R_d + \rho_v R_v) \frac{dT}{dt}. \end{aligned} \quad (\text{A19})$$

Now this leads to the temperature equation:

$$\rho_d(c_{vml} + R_m)\frac{dT}{dt} = \rho_d c_{pml}\frac{dT}{dt} = \frac{dp}{dt} - R_v T(S_v + S_{ph}) + (h_v - c_{vv}T - L_{00})S_v + (c_{pl}T - c_{vv}T - L_{00})S_{ph} - \frac{\partial}{\partial z}(\rho_r W_f e_l) - \rho_r W_f g, \quad (A20)$$

5 With $c_{pv} - c_{vv} = R_v$, the water vapor source term disappears:

$$(h_v - c_{vv}T - L_{00} - R_v T)S_v = (c_{pv}T + L_{00} - c_{vv}T - L_{00} - R_v T)S_v = 0. \quad (A21)$$

Further simplifying:

$$(c_{pl}T - c_{vv}T - R_v T - L_{00})S_{ph} = (c_{pl}T - c_{vv}T - R_v T - L_v + (c_{pv} - c_{pl})T)S_{ph} = -L_v S_{ph}. \quad (A22)$$

Rearranging finally leads to the temperature equation

$$\rho_d c_{pml}\frac{dT}{dt} = \frac{dp}{dt} - L_v S_{ph} - \frac{\partial}{\partial z}(\rho_r W_f e_l) - \rho_r W_f g. \quad (A23)$$

15 and its logarithmic derivative

$$\frac{d \ln T}{dt} = \frac{R_m}{c_{pml}} \frac{d \ln p}{dt} - \frac{L_v}{\rho_d c_{pml} T} S_{ph} - \frac{1}{\rho_d c_{pml} T} \frac{\partial}{\partial z}(\rho_r W_f e_l) - \frac{\rho_r W_f g}{\rho_d c_{pml} T}. \quad (A24)$$

A2 Potential temperature

20 A prognostic equation for the (moist) potential temperature is derived here. This is necessary because it appears in the density potential temperature equation later on. Quantities that contain water vapor and liquid water are marked with a tilde to distinguish them from their dry equivalents (e.g. dry potential temperature θ).

The moist potential temperature is

$$\tilde{\theta} = \frac{T}{\tilde{\pi}} \quad \text{with} \quad \tilde{\pi} = \left(\frac{\rho}{\rho_0} \right)^{\frac{R_m}{c_{pml}}}. \quad (\text{A25})$$

Taking the logarithm of the Exner function $\tilde{\pi}$ leads to

$$\ln \tilde{\pi} = \frac{R_m}{c_{pml}} \ln \left(\frac{\rho}{\rho_0} \right). \quad (\text{A26})$$

The time derivative is

$$\begin{aligned} \frac{d \ln \tilde{\pi}}{dt} &= \frac{R_v}{R_m} \ln \tilde{\pi} \frac{dr_v}{dt} - \frac{\ln \tilde{\pi}}{c_{pml}} \left(c_{pv} \frac{dr_v}{dt} + c_{pl} \frac{dr_l}{dt} \right) + \frac{R_m}{c_{pml}} \frac{d \ln \rho}{dt} \\ &= \frac{R_v}{R_m} \ln \tilde{\pi} \frac{S_v + S_{ph}}{\rho_d} - \ln \tilde{\pi} \left(\frac{c_{pv}}{c_{pml}} \frac{S_v + S_{ph}}{\rho_d} - \frac{c_{pl}}{c_{pml}} \frac{S_{ph} + S_{fall}}{\rho_d} \right) + \frac{R_m}{c_{pml}} \frac{d \ln \rho}{dt} \\ &= \ln \tilde{\pi} \left(\left[\frac{R_v}{R_m} - \frac{c_{pv}}{c_{pml}} \right] \frac{S_v + S_{ph}}{\rho_d} + \frac{c_{pl}}{c_{pml}} \frac{S_{ph} + S_{fall}}{\rho_d} \right) + \frac{R_m}{c_{pml}} \frac{d \ln \rho}{dt} \\ &= \frac{\ln \tilde{\pi}}{\rho_d} \left(\frac{R_v}{R_m} - \frac{c_{pv}}{c_{pml}} \right) S_v + \frac{\ln \tilde{\pi}}{\rho_d} \left(\frac{R_v}{R_m} + \frac{c_{pl} - c_{pv}}{c_{pml}} \right) S_{ph} \\ &\quad + \frac{\ln \tilde{\pi}}{\rho_d} \frac{c_{pl}}{c_{pml}} S_{fall} + \frac{R_m}{c_{pml}} \frac{d \ln \rho}{dt}, \end{aligned} \quad (\text{A27})$$

which leads us to the moist potential temperature equation:

$$\begin{aligned} \frac{d \ln \tilde{\theta}}{dt} &= \frac{d \ln T}{dt} - \frac{d \ln \tilde{\pi}}{dt} \\ &= \frac{R_m}{c_{pml}} \frac{d \ln \rho}{dt} - \frac{L_v}{\rho_d c_{pml} T} S_{ph} - \frac{1}{\rho_d c_{pml} T} \frac{\partial}{\partial z} (\rho_r W_f e_1) - \frac{\rho_r W_f g}{\rho_d c_{pml} T} \end{aligned}$$



$$\begin{aligned}
& -\frac{\ln \tilde{\pi}}{\rho_d} \left(\frac{R_v}{R_m} - \frac{c_{pv}}{c_{pml}} \right) S_v - \frac{\ln \tilde{\pi}}{\rho_d} \left(\frac{R_v}{R_m} + \frac{c_{pl} - c_{pv}}{c_{pml}} \right) S_{ph} - \frac{\ln \tilde{\pi}}{\rho_d} \frac{c_{pl}}{c_{pml}} S_{fall} - \frac{R_m}{c_{pml}} \frac{d \ln p}{dt} \\
& = -\frac{\ln \tilde{\pi}}{\rho_d} \left(\frac{R_v}{R_m} - \frac{c_{pv}}{c_{pml}} \right) S_v - \frac{1}{\rho_d} \left(\frac{L_v}{c_{pml} T} + \ln \tilde{\pi} \left[\frac{R_v}{R_m} + \frac{c_{pl} - c_{pv}}{c_{pml}} \right] \right) S_{ph} \\
& - \frac{\ln \tilde{\pi}}{\rho_d} \frac{c_{pl}}{c_{pml}} S_{fall} - \frac{1}{\rho_d c_{pml} T} \frac{\partial}{\partial z} (\rho_r W_f e_1) - \frac{\rho_r W_f g}{\rho_d c_{pml} T}. \tag{A28}
\end{aligned}$$

5 A3 Density potential temperature

With the definition of the density potential temperature

$$\theta_\rho = \tilde{\theta} \frac{1 + r_v / \varepsilon}{1 + r_v + r_1} \tag{A29}$$

and by using the product rule:

$$\begin{aligned}
\frac{d\theta_\rho}{dt} & = \frac{1 + r_v / \varepsilon}{1 + r_v + r_1} \frac{d\tilde{\theta}}{dt} + \frac{\tilde{\theta}}{1 + r_v + r_1} \frac{1}{\varepsilon} \frac{dr_v}{dt} - \tilde{\theta} \frac{1 + r_v / \varepsilon}{(1 + r_v + r_1)^2} \left(\frac{dr_v}{dt} + \frac{dr_1}{dt} \right) \\
& = \frac{\theta_\rho}{\tilde{\theta}} \frac{d\tilde{\theta}}{dt} + \theta_\rho \left(\frac{1}{\varepsilon + r_v} - \frac{1}{1 + r_v + r_1} \right) \frac{dr_v}{dt} - \frac{\theta_\rho}{1 + r_v + r_1} \frac{dr_1}{dt}. \tag{A30}
\end{aligned}$$

Inserting Eqs. (A28), (A5) and (A6) in Eq. (A30):

$$\begin{aligned}
\frac{d \ln \theta_\rho}{dt} & = \frac{d \ln \tilde{\theta}}{dt} + \left(\frac{1}{\varepsilon + r_v} - \frac{1}{1 + r_v + r_1} \right) \frac{dr_v}{dt} - \frac{1}{1 + r_v + r_1} \frac{dr_1}{dt} \\
& = -\frac{\ln \tilde{\pi}}{\rho_d} \left(\frac{R_v}{R_m} - \frac{c_{pv}}{c_{pml}} \right) S_v - \frac{1}{\rho_d} \left(\frac{L_v}{c_{pml} T} + \ln \tilde{\pi} \left[\frac{R_v}{R_m} + \frac{c_{pl} - c_{pv}}{c_{pml}} \right] \right) S_{ph} \\
& - \frac{\ln \tilde{\pi}}{\rho_d} \frac{c_{pl}}{c_{pml}} S_{fall} - \frac{1}{\rho_d c_{pml} T} \frac{\partial}{\partial z} (\rho_r W_f e_1) - \frac{\rho_r W_f g}{\rho_d c_{pml} T}
\end{aligned}$$

$$+ \left(\frac{1}{\varepsilon + r_v} - \frac{1}{1 + r_v + r_l} \right) \frac{S_v + S_{ph}}{\rho_d} + \frac{1}{1 + r_v + r_l} \frac{S_{ph} + S_{fall}}{\rho_d}. \quad (A31)$$

With the relation

$$\frac{1}{\varepsilon + r_v} = \frac{1}{\frac{R_d}{R_v} + r_v} = \frac{R_v}{R_d + r_v R_v} = \frac{R_v}{R_m} \quad (A32)$$

we get the density potential temperature equation sort by source terms:

$$\begin{aligned} \frac{d\theta_\rho}{dt} &= \frac{\theta_\rho}{\rho_d} \left(\frac{R_v}{R_m} - \frac{\rho_d}{\rho} - \ln \tilde{\pi} \left[\frac{R_v}{R_m} - \frac{c_{pv}}{c_{pml}} \right] \right) S_v \\ &+ \frac{\theta_\rho}{\rho_d} \left(\frac{R_v}{R_m} - \ln \tilde{\pi} \left[\frac{R_v}{R_m} + \frac{c_{pl} - c_{pv}}{c_{pml}} \right] - \frac{L_v}{c_{pml} T} \right) S_{ph} \\ &+ \frac{\theta_\rho}{\rho_d} \left(\frac{\rho_d}{\rho} - \frac{c_{pl}}{c_{pml}} \ln \tilde{\pi} \right) S_{fall} - \frac{\theta_\rho}{\rho_d c_{pml} T} \frac{\partial}{\partial z} (\rho_r W_r e_l) - \frac{\theta_\rho \rho_r W_r g}{\rho_d c_{pml} T}. \end{aligned} \quad (A33)$$

Appendix B: Soil and land use parameters

Varying ratios of silt, clay and sand significantly change the properties of soil and thus determine the heat and moisture fluxes of the surface. Accordingly, these different ratios are referred to specifically defined soil types. In the following Tables B1 and B2 parameters describing the physical properties of the appropriate soil type are listed. W_{pv} stands for the pore volume of the soil, W_{fc} is the field capacity (Eq. 72) describing a threshold value for runoff in the soil layers. κ_{sat} and Ψ_{sat} defines the hydraulic conductivity and the matric potential at saturation, respectively (Eqs. 69 and 70). $\rho_0 c_0$ is the heat capacity of dry soil as used in Eq. (74) and b^* is a parameter for the soil porosity.

Code availability and visualization

The ASAM code is managed with Git, a distributed revision control and source code management (SCM) system. To get access to the source code and additional scripts for pre- and postprocessing, a registration at the TROPOS Git hosting website <https://gitorious.tropos.de/> is mandatory. Additional information can be found at the ASAM webpage (<http://asam.tropos.de>).

As visualization tool, the free and open source software VisIt (<https://wci.llnl.gov/codes/visit/>) is used. VisIt can read over 120 scientific file formats and offers opportunity to include own scripts, if necessary. It is available for Unix, Windows and Mac workstations.

Acknowledgements. This work is internally funded by TROPOS. The authors like to thank the CGIAR-CSI for providing the high-resolution SRTM topography dataset. We are also grateful to our technical employees Sabine Reutgen and Birgit Heinrich for developing and maintaining the grid generator as well as data maintenance and converting, respectively.

References

- Bott, A.: Theoretical considerations on the mass and energy consistent treatment of precipitation in cloudy atmospheres, *Atmos. Res.*, 89, 262–269, 2008. 4494
- Braun, F. J.: Mesoskalige Modellierung der Bodenhydrologie, *Wiss. Berichte des Inst. f. Meteor. u. Klimat. d. Universität Karlsruhe*, 30, 2002. 4483, 4484
- Bryan, G. H. and Fritsch, J. M.: A benchmark simulation for moist nonhydrostatic numerical models, *Mon. Weather Rev.*, 130, 2917–2928, 2002. 4466, 4486, 4487, 4488
- Chen, F. and Dudhia, J.: Coupling an advanced land surface–hydrology model with the Penn State-NCAR MM5 modeling system. Part I: Model implementation and sensitivity, *Mon. Weather Rev.*, 129, 569–585, 2001. 4485
- Cheng, Y. and Brutsaert, W.: Flux-profile relationships for wind speed and temperature in the stable atmospheric boundary layer, *Bound.-Lay. Meteorol.*, 114, 519–53, 2005. 4483
- Deardorff, J. W.: Numerical investigation of neutral und unstable boundary layers, *J. Atmos. Sci.*, 29, 91–115, 1972. 4475, 4476

GMDD

7, 4463–4525, 2014

ASAM v2.7

M. Jähn et al.

Title Page

Abstract

Introduction

Conclusions

References

Tables

Figures

◀

▶

◀

▶

Back

Close

Full Screen / Esc

Printer-friendly Version

Interactive Discussion



[Title Page](#)[Abstract](#)[Introduction](#)[Conclusions](#)[References](#)[Tables](#)[Figures](#)[Back](#)[Close](#)[Full Screen / Esc](#)[Printer-friendly Version](#)[Interactive Discussion](#)

Doms, G., Förstner, J., Heise, E., Herzog, H.-J., Mironov, D., Raschendorfer, M., Reinhardt, T., Ritter, B., Schrodin, R., Schulz, J.-P., and Vogel, G.: A Description of the Nonhydrostatic Regional COSMO Model, *Deutscher Wetterdienst*, 2011. 4472, 4479, 4482, 4483, 4484, 4510

5 Emanuel, K. A.: *Atmospheric Convection*, Oxford University Press, 1994. 4467

Engelmann, R., Ansmann, A., Horn, S., Seifert, P., Althausen, D., Tesche, M., Esselborn, M., Fruntke, J., Lieke, K., Freudenthaler, V., and Gross, S.: Doppler lidar studies of heat island effects on vertical mixing of aerosols during SAMUM-2, *Tellus B*, 63, 448–458, 2011. 4489

10 Fairall, C. W., Bradley, E. F., Rogers, D. P., Edson, J. B., and Young, G. S.: Bulk parameterization of air-sea fluxes for Tropical Ocean Global Atmosphere Coupled-Ocean Atmosphere Response Experiment, *J. Geophys. Res.*, 101, 3747–3764, 1996. 4483

Hicken, J., Ham, F., Militzer, J., and Koksals, M.: A shift transformation for fully conservative methods: turbulence simulation on complex, unstructured grids, *J. Comput. Phys.*, 208, 704–714, 2005. 4470

15 Horn, S.: ASAMgpu V1.0 – a moist fully compressible atmospheric model using graphics processing units (GPUs), *Geosci. Model Dev.*, 5, 345–353, doi:10.5194/gmd-5-345-2012, 2012. 4465, 4478

Hundsdoerfer, W., Koren, B., Loon, M. V., and Verwer, J. G.: A positive finite-difference advection scheme, *J. Comput. Phys.*, 117, 35–46, 1995. 4469

20 Jebens, S., Knoth, O., and Weiner, R.: Partially implicit peer methods for the compressible Euler equations, *J. Comput. Phys.*, 230, 4955–4974, 2011. 4471

Jiménez, P. A., Dudhia, J., González-Rouco, J. F., Navarro, J., Montávez, J. P., and García-Bustamante, E.: A revised scheme for the WRF surface layer formulation, *Mon. Weather Rev.*, 140, 898–918, 2012. 4482, 4483

25 Kleissl, J., Kumar, V., Meneveau, C., and Parlange, M. B.: Numerical study of dynamic Smagorinsky models in large-eddy simulation of the atmospheric boundary layer: validation in stable and unstable conditions, *Water Resour. Res.*, 42, W06D10, doi:10.1029/2005WR004685, 2006. 4493

König, M.: Large-eddy simulation modelling for urban Scale, Ph.D. thesis, University of Leipzig, 2013. 4465

30 Knoth, O. and Wensch, J.: Generalized split-explicit Runge–Kutta methods for the compressible Euler equations, *Mon. Weather Rev.*, 142, 2067–2081, 2014. 4474

[Title Page](#)[Abstract](#)[Introduction](#)[Conclusions](#)[References](#)[Tables](#)[Figures](#)[⏪](#)[⏩](#)[◀](#)[▶](#)[Back](#)[Close](#)[Full Screen / Esc](#)[Printer-friendly Version](#)[Interactive Discussion](#)

- Kong, L. C., Tunçel, L., and Xiu, N. H.: The Fischer–Burmeister complementarity function on Euclidean Jordan algebras, *Pac. J. Optim.*, 6, 423–440, 2010. 4478
- Lanser, D., Blom, J. G., and Verwer, J. G.: Time integration of the shallow water equations in spherical geometry, *J. Comput. Phys.*, 171, 373–393, 2001. 4471
- 5 Lilly, D. K.: The representation of small scale turbulence in numerical simulation experiments, IBM Scientific Computing Symposium on environmental sciences, 195–210, 1967. 4475
- Lock, S.-J., Bitzer, H.-W., Coals, A., Gadian, A., and Mobbs, S.: Demonstration of a cut-cell representation of 3D orography for studies of atmospheric flows over very steep hills, *Mon. Weather Rev.*, 140, 411–424, 2012. 4464
- 10 McCumber, M. D.: A numerical simulation of the influence of heat and moisture fluxes upon mesoscale circulation, Ph.D. thesis, Dept. of Environmental Science, University of Virginia, Charlottesville, VA, 1980. 4511
- Noilhan, J. and Planton, S.: A simple parameterization of land surface processes for meteorological models, *Mon. Weather Rev.*, 117, 536–549, 1989. 4484
- 15 Pielke, R. A.: *Mesoscale Meteorological Modeling*, 2nd Edn., Academic Press, 1984. 4485, 4511
- Porté-Agel, F., Meneveau, C., and Parlange, M. B.: A scale-dependent dynamic model for large-eddy simulation: application to a neutral atmospheric boundary layer, *J. Fluid Mech.*, 415, 261–284, 2000. 4493
- 20 Satoh, M., Matsuno, T., Tomita, H., Miura, H., Nasuno, T., and Iga, S.: Nonhydrostatic icosahedral atmospheric model (NICAM) for global cloud resolving simulations, *J. Comput. Phys.*, 227, 3486–3514, 2008. 4494
- Savijärvi, H. and Matthews, S.: Flow over small heat islands: a numerical sensitivity study, *J. Atmos. Sci.*, 61, 859–868, 2004. 4492
- 25 Schaer, C., Leuenberger, D., Fuhrer, O., Lüthi, D., and Girard, C.: A new terrain-following vertical coordinate formulation for atmospheric prediction models, *Mon. Weather Rev.*, 130, 2459–2480, 2002. 4466, 4486, 4488
- Scotti, A., Meneveau, C., and Lilly, D. K.: Generalized Smagorinsky model for anisotropic grids, *Phys. Fluids A-Fluid*, 5, 2306–2308, 1993. 4476
- 30 Seifert, A. and Beheng, K. D.: A two-moment cloud microphysics parameterization for mixed-phase clouds, *Meteorol. Atmos. Phys.*, 92, 45–66, 2006. 4477, 4478

[Title Page](#)[Abstract](#)[Introduction](#)[Conclusions](#)[References](#)[Tables](#)[Figures](#)[Back](#)[Close](#)[Full Screen / Esc](#)[Printer-friendly Version](#)[Interactive Discussion](#)

Skamarock, W. C., Klemp, J. B., Dudhia, J., Gill, D. O., Barker, M., Duda, K. G., Huang, X. Y., Wang, W., and Powers, J. G.: A description of the Advanced Research WRF Version 3, Tech. rep., National Center for Atmospheric Research, 2008. 4471

Smagorinsky, J.: General circulation experiments with the primitive equations, *Mon. Weather Rev.*, 164, 91–99, 1963. 4475

Stappeler, J., Bitzer, H.-W., Minotte, M., and Bonaventura, L.: Nonhydrostatic atmospheric modeling using a z-coordinate representation, *Mon. Weather Rev.*, 130, 2143–2149, 2002. 4465

Straka, J. M., Wilhelmson, R. B., Wicker, L. J., Anderson, J. R., and Droegemeier, K. K.: Numerical solutions of a non-linear density current: a benchmark solution and comparisons, *Int. J. Numer. Meth. Fl.*, 17, 1–22, 1993. 4466, 4486

Sweby, P. K.: High resolution schemes using flux limiters for hyperbolic conservation laws, *SIAM J. Numer. Anal.*, 21, 995–1011, 1984. 4469

Tripoli, G. J. and Smith, E. A.: Introducing Variable-Step Topography (VST) coordinates within dynamically constrained Nonhydrostatic Modeling System (NMS). Part 1: VST formulation within NMS host model framework, *Dynam. Atmos. Oceans*, 66, 28–57, 2014a. 4464

Tripoli, G. J. and Smith, E. A.: Introducing Variable-Step Topography (VST) coordinates within dynamically constrained Nonhydrostatic Modeling System (NMS). Part 2: VST performance on orthodox obstacle flows, *Dynam. Atmos. Oceans*, 66, 10–27, 2014b. 4465

Van Genuchten, M. T.: A closed-form equation for predicting the hydraulic conductivity of unsaturated soils, *Soil Sci. Soc. Am. J.*, 44, 892–898, 1980. 4483

Van Leer, B.: Upwind-difference methods for aerodynamic problems governed by the Euler equations, in: *Lectures in Applied Mathematics*, 327–336, 1994. 4468

Walko, R. L. and Avissar, R.: The Ocean–Land–Atmosphere Model (OLAM). Part I: Shallow-water tests, *Mon. Weather Rev.*, 136, 4033–4044, 2008a. 4465

Walko, R. L. and Avissar, R.: The Ocean–Land–Atmosphere Model (OLAM). Part II: Formulation and tests of the nonhydrostatic dynamic core, *Mon. Weather Rev.*, 136, 4045–4062, 2008b. 4465

Wensch, J., Knoth, O., and Galant, A.: Multirate infinitesimal step methods for atmospheric flow simulation, *BIT Numerical Mathematics*, 49, 449–473, 2009. 4474

Wicker, L. J. and Skamarock, W. C.: A time-splitting scheme for the elastic equations incorporating second-order Runge–Kutta time differencing, *Mon. Weather Rev.*, 126, 1992–1999, 1998. 4487

[Title Page](#)[Abstract](#)[Introduction](#)[Conclusions](#)[References](#)[Tables](#)[Figures](#)[◀](#)[▶](#)[◀](#)[▶](#)[Back](#)[Close](#)[Full Screen / Esc](#)[Printer-friendly Version](#)[Interactive Discussion](#)**Table 1.** Physical constants.

Symbol	Quantity	Value
p_0	Reference pressure	10^5 Pa
R_d	Gas constant for dry air	$287 \text{ J kg}^{-1} \text{ K}^{-1}$
R_v	Gas constant for water vapor	$461 \text{ J kg}^{-1} \text{ K}^{-1}$
c_{pd}	Specific heat capacity at constant pressure for dry air	$1004 \text{ J kg}^{-1} \text{ K}^{-1}$
c_{pv}	Specific heat capacity at constant pressure for water vapor	$1885 \text{ J kg}^{-1} \text{ K}^{-1}$
c_{pl}	Specific heat capacity at constant pressure for liquid water	$4186 \text{ J kg}^{-1} \text{ K}^{-1}$
c_{vd}	Specific heat capacity at constant volume for dry air	$717 \text{ J kg}^{-1} \text{ K}^{-1}$
c_{vv}	Specific heat capacity at constant volume for water vapor	$1424 \text{ J kg}^{-1} \text{ K}^{-1}$
L_{00}	Latent heat at 0 K	$3.148 \times 10^6 \text{ J kg}^{-1}$
g	Gravitational acceleration	9.81 m s^{-2}
C_s	Smagorinsky coefficient	0.2

GMDD

7, 4463–4525, 2014

ASAM v2.7

M. Jähn et al.

Title Page

Abstract

Introduction

Conclusions

References

Tables

Figures



Back

Close

Full Screen / Esc

Printer-friendly Version

Interactive Discussion

**Table 2.** Coefficient table for ROS2.

0 2/3		
-5/4 3/4	-4/3	$\frac{1}{2} + \frac{1}{6}\sqrt{3}$
A-Matrix	Γ-Matrix	γ

GMDD

7, 4463–4525, 2014

ASAM v2.7

M. Jähn et al.

Title Page

Abstract

Introduction

Conclusions

References

Tables

Figures



Back

Close

Full Screen / Esc

Printer-friendly Version

Interactive Discussion

**Table 3.** Coefficient table for ROSRK3

0	0	
1/3	-11/27	1
11/54 1/2	17/27 -11/4	
-17/27 11/4 1		
\mathcal{A} -Matrix	Γ -Matrix	γ

[Title Page](#)[Abstract](#)[Introduction](#)[Conclusions](#)[References](#)[Tables](#)[Figures](#)[Back](#)[Close](#)[Full Screen / Esc](#)[Printer-friendly Version](#)[Interactive Discussion](#)**Table 4.** LES model configuration for the Barbados sensitivity study.

	Model parameter
Domain	110 km × 110 km × 6 km
Grid cells	256 × 256 × 38
Lateral boundary conditions	Inflow (E)/outflow (N,S,W)
Start time (LT)	00:00
Integration time	24 h
Topography data	SRTM, 100 m resolution
Turbulence scheme	Standard Smagorinsky
Cloud microphysics	Warm 2-moment bulk scheme
Surface fluxes	Constant flux layer

[Title Page](#)[Abstract](#)[Introduction](#)[Conclusions](#)[References](#)[Tables](#)[Figures](#)[Back](#)[Close](#)[Full Screen / Esc](#)[Printer-friendly Version](#)[Interactive Discussion](#)**Table 5.** Overview of the performed simulation cases in the Barbados sensitivity study.

Label	Topography	u_0 (m s^{-1})	v_0 (m s^{-1})	RH_0 (%)
REF	yes	−10	0	70
FLAT	no	−10	0	70
U05	yes	−5	0	70
RH80	yes	−10	0	80

Table B1. Soil parameters from Doms et al. (2011).

Soil type	W_{pv} [$\text{m}^3 \text{m}^{-3}$]	W_{fc} [$\text{m}^3 \text{m}^{-3}$]	κ_{sat} [m s^{-1}]	$\rho_0 c_0$ [$\text{W} (\text{m}^3 \text{K})^{-1}$]	b^* ^a
Sand	0.364	0.196	4970×10^{-8}	1.28×10^6	3.5
Sandy loam	0.445	0.260	943×10^{-8}	1.35×10^6	4.8
Loam	0.455	0.340	531×10^{-8}	1.42×10^6	6.1
Clay loam	0.475	0.370	764×10^{-8}	1.50×10^6	8.6
Clay	0.507	0.463	1.7×10^{-8}	1.63×10^6	10.0
Peat	0.863	0.763	5.8×10^{-8}	0.58×10^6	9.0

^a with $n = 1/b^* + 1$, see Eqs. (69) and (70).

[Title Page](#)
[Abstract](#)
[Introduction](#)
[Conclusions](#)
[References](#)
[Tables](#)
[Figures](#)
[Back](#)
[Close](#)
[Full Screen / Esc](#)
[Printer-friendly Version](#)
[Interactive Discussion](#)


Table B2. Soil parameters as used in Pielke (1984) (adapted from McCumber, 1980).

Soil type	W_{pv} [$\text{m}^3 \text{m}^{-3}$]	Ψ_{sat} [m]	κ_{sat} [m s^{-1}]	$\rho_0 c_0$ [$\text{W}(\text{m}^3 \text{K})^{-1}$]	b^* ^a
Sand	0.395	-0.121	1760×10^{-8}	1.47×10^6	4.05
Sandy Loam	0.435	-0.218	341×10^{-8}	1.34×10^6	4.90
Loam	0.451	-0.478	70×10^{-8}	1.21×10^6	5.39
Clay loam	0.476	-0.630	25×10^{-8}	1.23×10^6	8.52
Clay	0.482	-0.405	13×10^{-8}	1.09×10^6	11.40
Peat	0.863	-0.356	80×10^{-8}	0.84×10^6	7.75

^a with $n = 1/b^* + 1$, see Eqs. (69) and (70).

[Title Page](#)
[Abstract](#)
[Introduction](#)
[Conclusions](#)
[References](#)
[Tables](#)
[Figures](#)
[Back](#)
[Close](#)
[Full Screen / Esc](#)
[Printer-friendly Version](#)
[Interactive Discussion](#)


GMDD

7, 4463–4525, 2014

ASAM v2.7

M. Jähn et al.

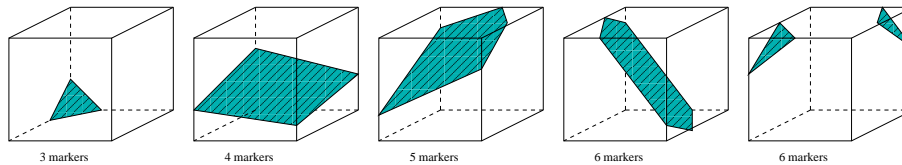


Figure 1. Possible configurations for cut cell intersection. The last two cases are excluded.

Title Page

Abstract

Introduction

Conclusions

References

Tables

Figures



Back

Close

Full Screen / Esc

Printer-friendly Version

Interactive Discussion



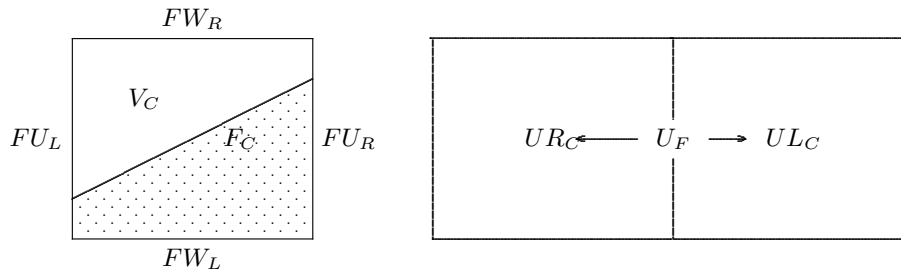


Figure 2. Cut cell with face and volume area information (left) and arrangement of face and cell centered momentum (right).

Title Page

Abstract

Introduction

Conclusions

References

Tables

Figures

◀

▶

◀

▶

Back

Close

Full Screen / Esc

Printer-friendly Version

Interactive Discussion



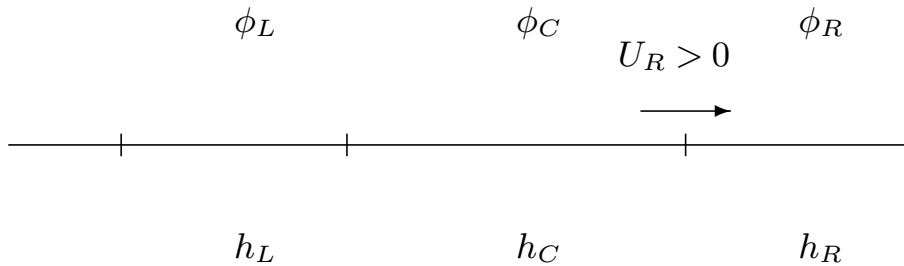


Figure 3. Stencil for third-order approximation.

GMDD

7, 4463–4525, 2014

ASAM v2.7

M. Jähn et al.

Title Page

Abstract

Introduction

Conclusions

References

Tables

Figures

◀

▶

◀

▶

Back

Close

Full Screen / Esc

Printer-friendly Version

Interactive Discussion



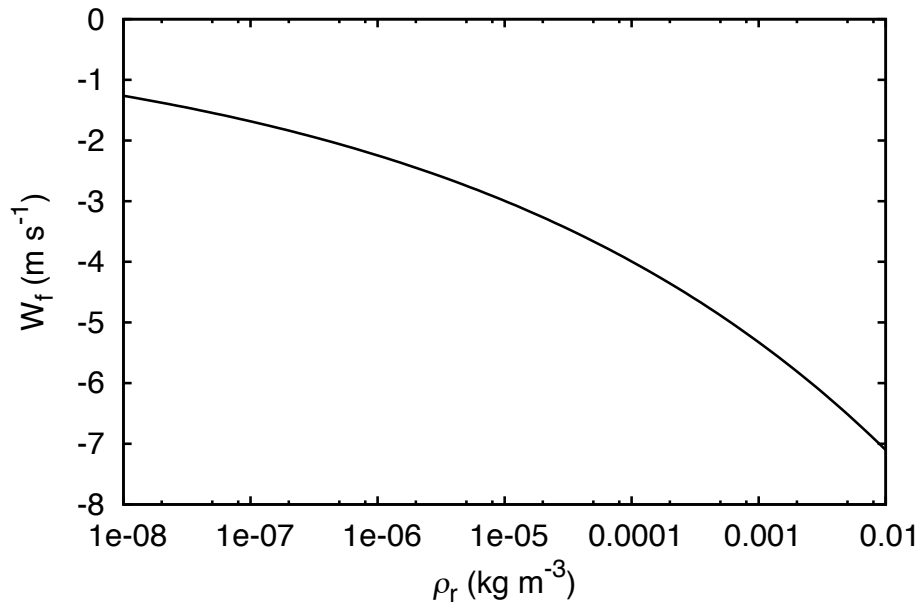


Figure 4. Terminal fall velocity of raindrops after Eq. (52).

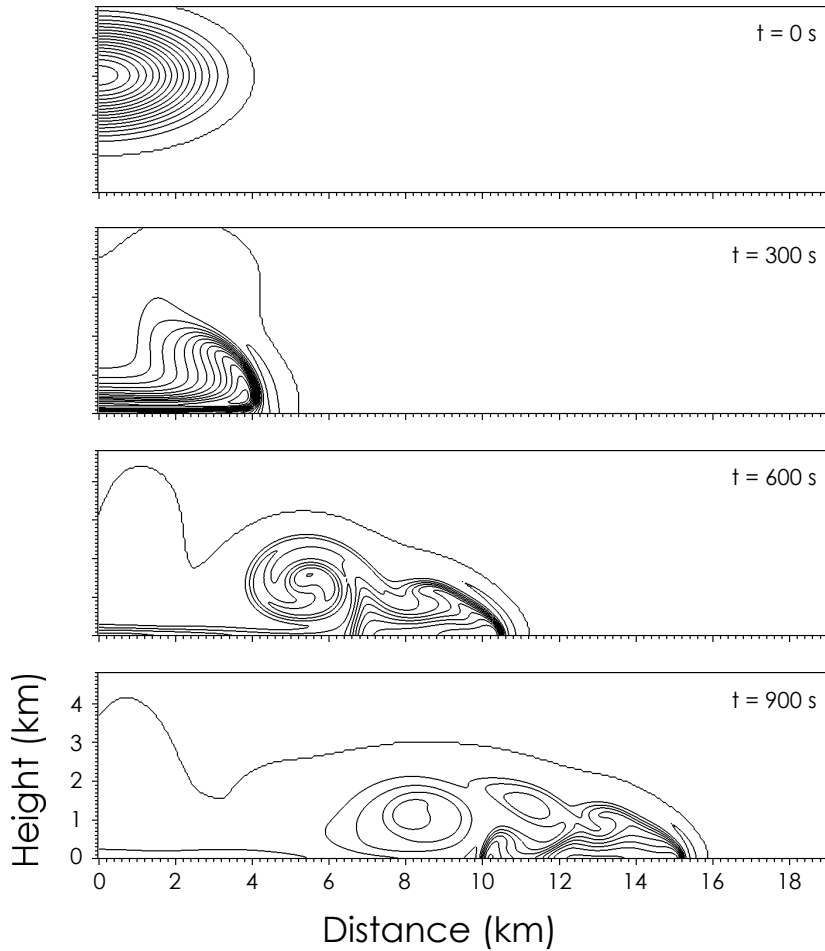


Figure 5. Perturbation potential temperature isolines (contour interval 2 K) at different times. Since the result is symmetric, only the right part of the model domain is shown.

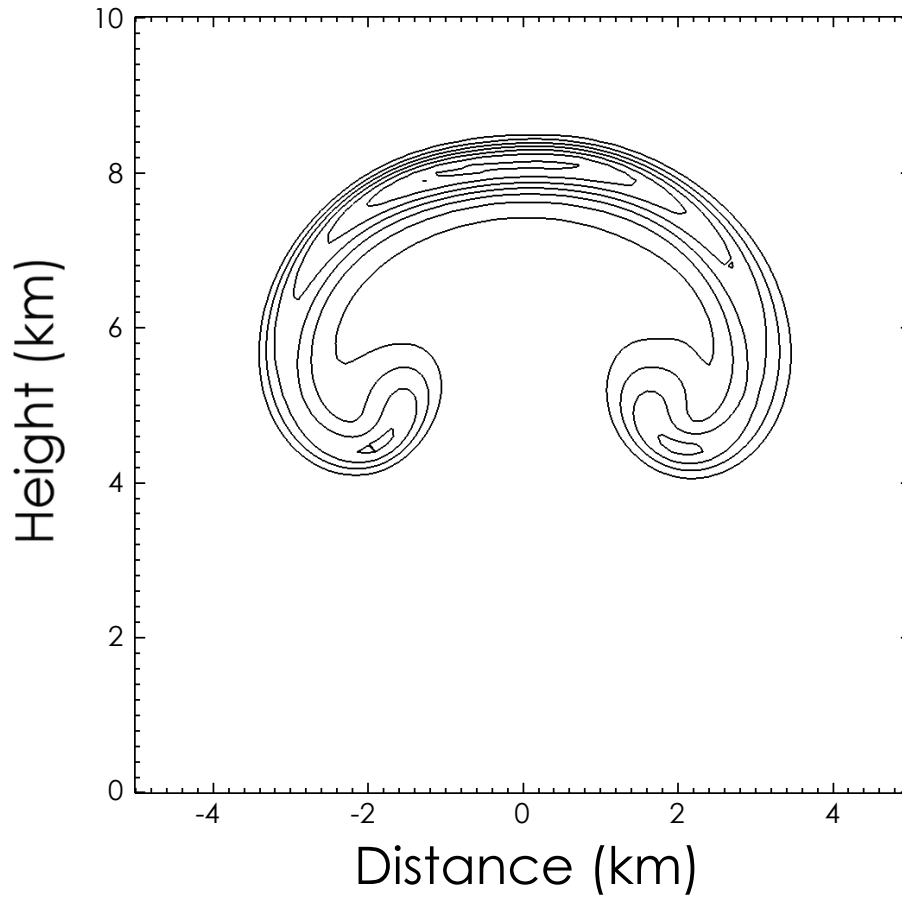


Figure 6. Perturbation equivalent potential temperature isolines (contour interval 0.5 K) at $t = 1000$ s.

Title Page

Abstract

Introduction

Conclusions

References

Tables

Figures



Back

Close

Full Screen / Esc

Printer-friendly Version

Interactive Discussion



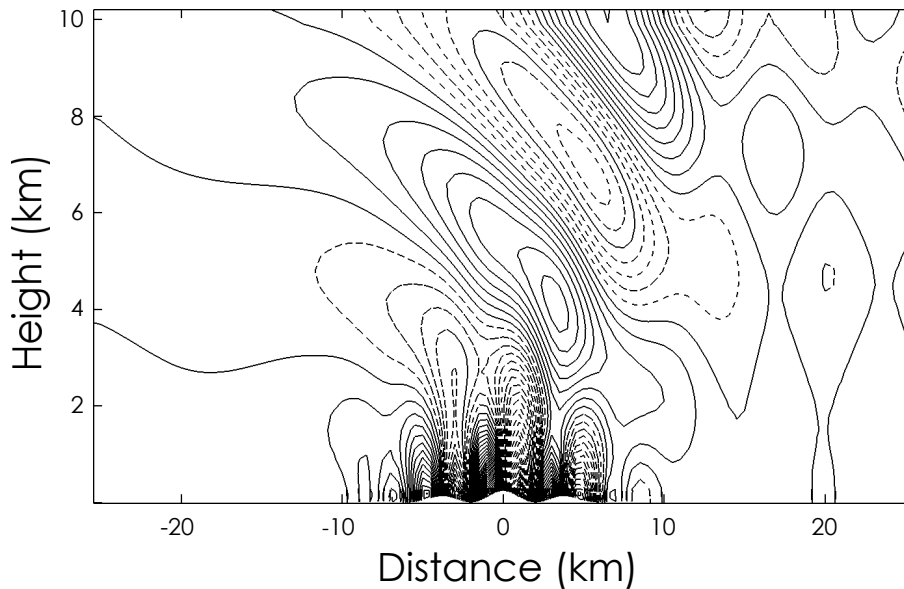


Figure 7. Steady state solution of the vertical velocity field (contour interval 0.05 m s^{-1} , negative contours dashed) at $t = 7200 \text{ s}$.

Title Page

Abstract

Introduction

Conclusions

References

Tables

Figures

◀

▶

◀

▶

Back

Close

Full Screen / Esc

Printer-friendly Version

Interactive Discussion



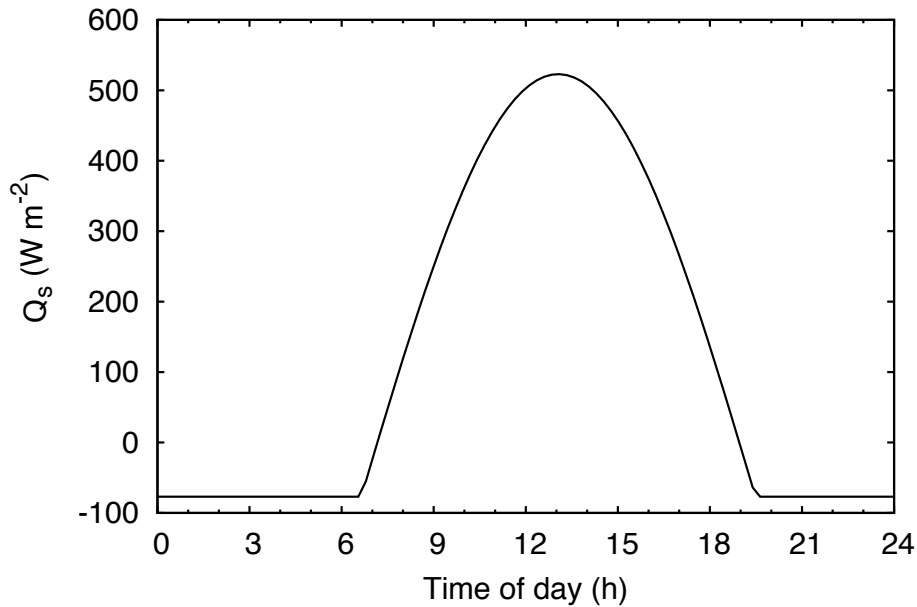


Figure 8. Model parameterization for the sensible surface heat flux over Barbados after Eq. (84).

Title Page

Abstract

Introduction

Conclusions

References

Tables

Figures



Back

Close

Full Screen / Esc

Printer-friendly Version

Interactive Discussion



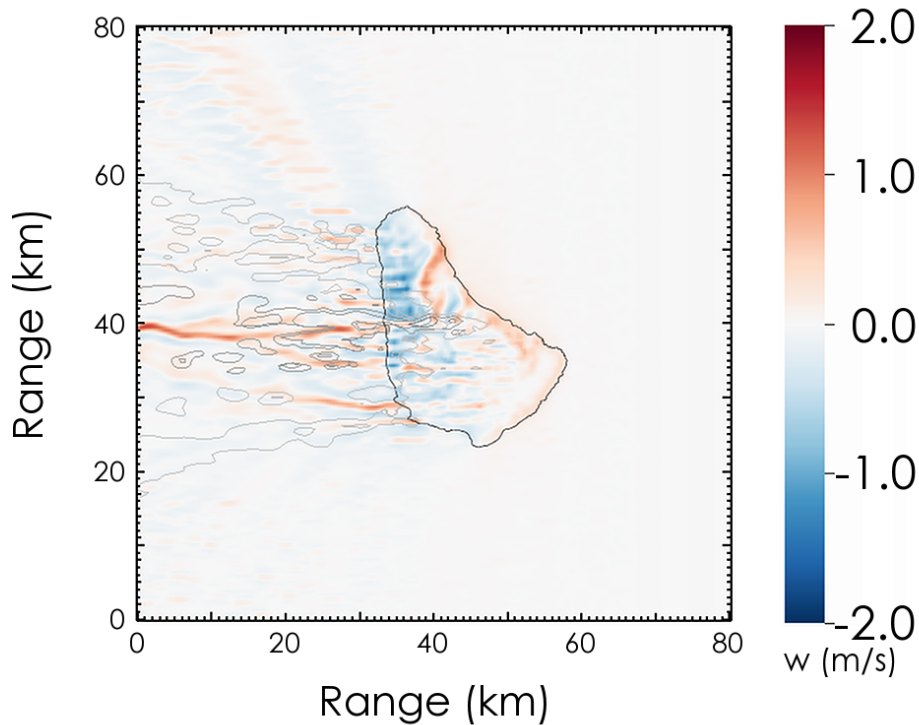


Figure 9. Snapshot at 14:00 LT for the vertical velocity field and density potential temperature isolines (lowest value 302.5 K in light grey, darker lines for higher values, contour interval 0.5 K) at 400 m height asl for the REF case simulation.

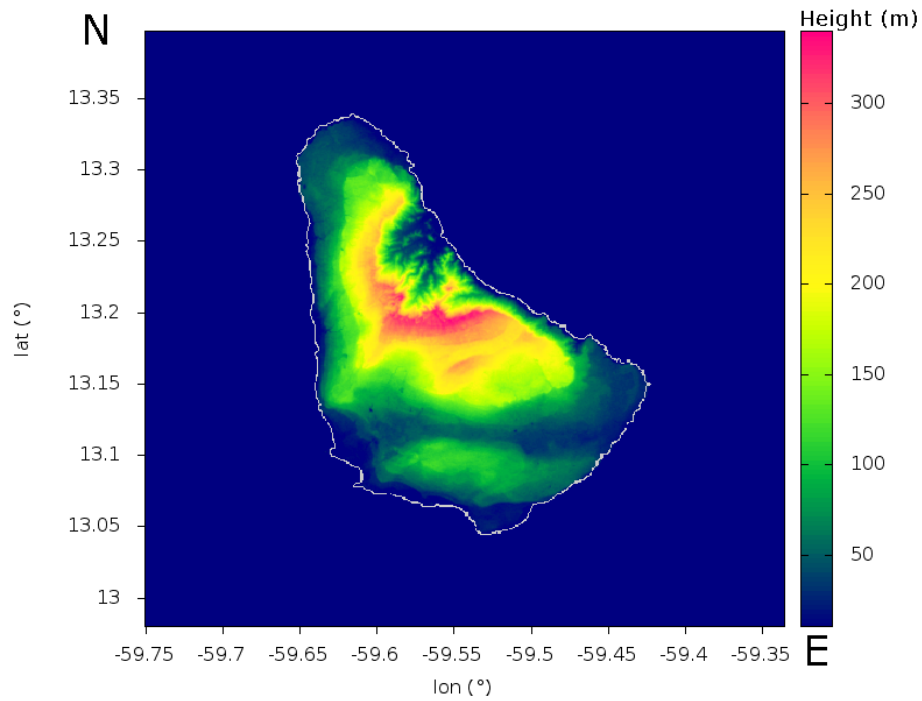


Figure 10. Topographic map of Barbados (SRTM output).

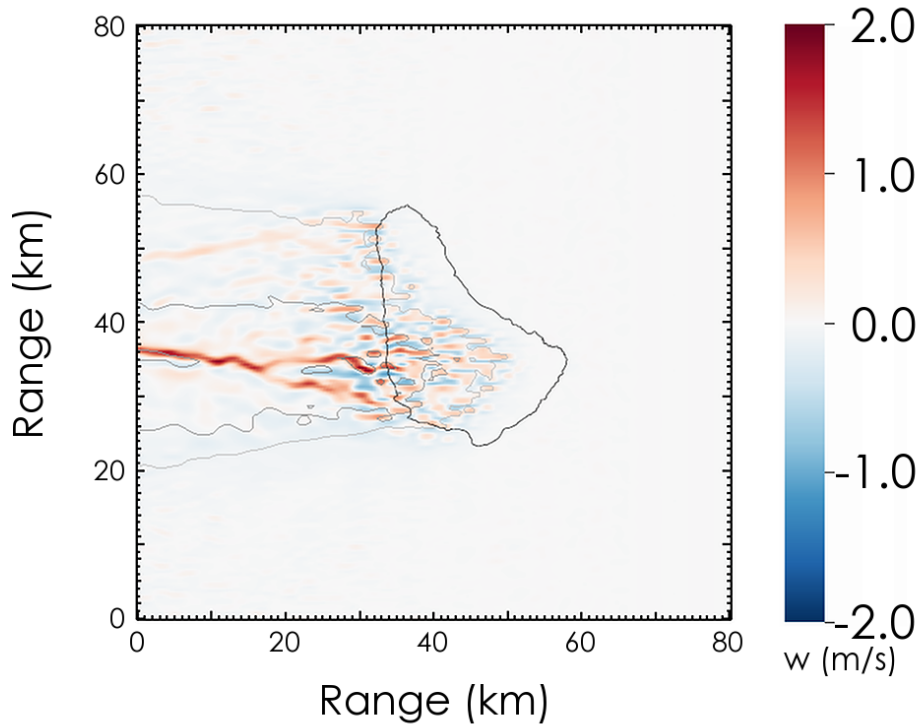


Figure 11. Same as Fig. 9, but for the FLAT case simulation.

Title Page

Abstract

Introduction

Conclusions

References

Tables

Figures

◀

▶

◀

▶

Back

Close

Full Screen / Esc

Printer-friendly Version

Interactive Discussion



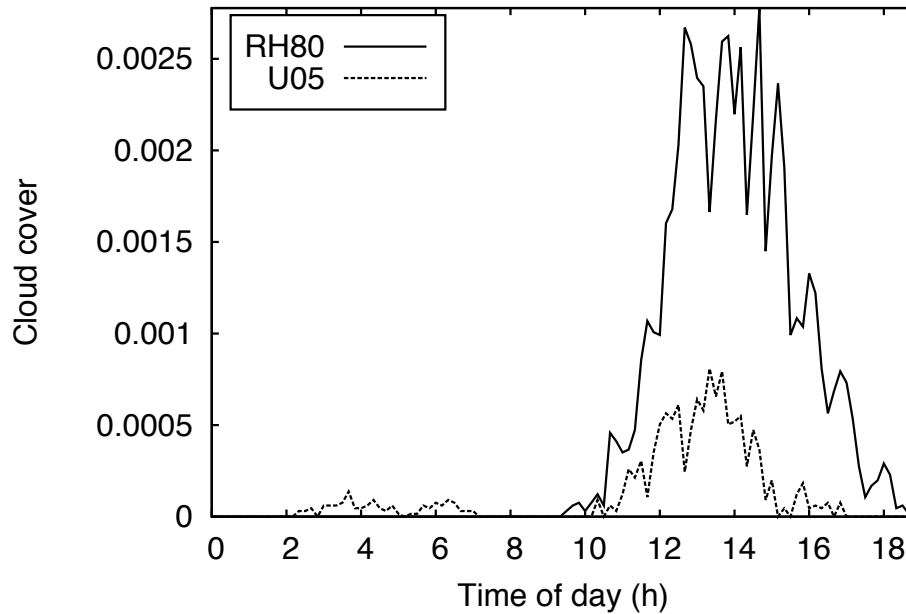


Figure 12. Time series of total cloud cover for the RH80 and U05 cases.

[Title Page](#)[Abstract](#)[Introduction](#)[Conclusions](#)[References](#)[Tables](#)[Figures](#)[◀](#)[▶](#)[◀](#)[▶](#)[Back](#)[Close](#)[Full Screen / Esc](#)[Printer-friendly Version](#)[Interactive Discussion](#)

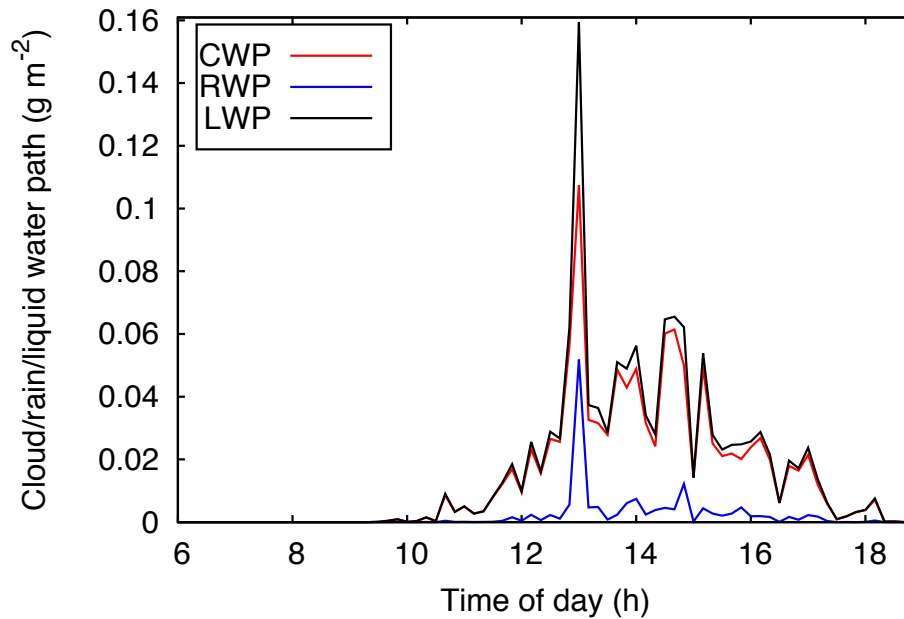


Figure 13. Time series of domain averaged cloud, rain and liquid water path for the RH80 case.

Title Page

Abstract

Introduction

Conclusions

References

Tables

Figures

◀

▶

◀

▶

Back

Close

Full Screen / Esc

Printer-friendly Version

Interactive Discussion



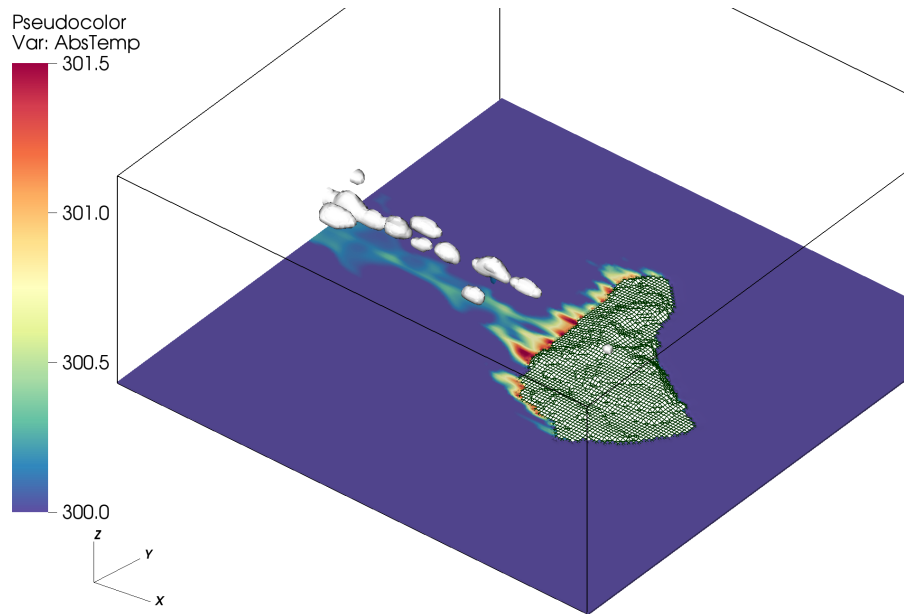


Figure 14. RH80 case: cloud field visualization for the island surrounded area at 14:40 LT. Isosurfaces of specific cloud water content of $q_c = 0.1 \text{ g kg}^{-1}$ as well as cut cells around the island orography and the lowest-level temperature field are shown.

Title Page

Abstract

Introduction

Conclusions

References

Tables

Figures

◀

▶

◀

▶

Back

Close

Full Screen / Esc

Printer-friendly Version

Interactive Discussion

